Ferromagnetic cluster-glass phase in $Ca(Co_{1-x}Ir_x)_{2-y}As_2$ crystals

Santanu Pakhira,[1] N. S. Sangeetha,[1] V. Smetana,[2] A.-V. Mudring,[2] and D. C. Johnston[1,3]

[1]*Ames Laboratory, Ames, Iowa 50011, USA*

[2]*Department of Materials and Environmental Chemistry, Stockholm University, Svante Arrhenius väg 16 C, 106 91 Stockholm, Sweden*

[3]*Department of Physics and Astronomy, Iowa State University, Ames, Iowa 50011, USA*

(Received 22 April 2020; revised 22 June 2020; accepted 23 June 2020; published 7 July 2020)

Single crystals of $Ca(Co_{1-x}Ir_x)_{2-y}As_2$ with $0 \leqslant x \leqslant 0.35$ and $0.10 \leqslant y \leqslant 0.14$ have been grown using the self-flux technique and characterized by single-crystal x-ray diffraction (XRD), energy-dispersive x-ray spectroscopy, magnetization M, and magnetic susceptibility χ measurements versus temperature T, magnetic field H, and time t, and heat-capacity $C_p(H,T)$ measurements. The XRD refinements reveal that all the Ir-substituted crystals crystallize in a collapsed-tetragonal structure as does the parent $CaCo_{2-y}As_2$ compound. A small 3.3% Ir substitution for Co in $CaCo_{1.86}As_2$ drastically lowers the A-type antiferromagnetic (AFM) transition temperature T_N from 52 to 23 K with a significant enhancement of the Sommerfeld electronic heat-capacity coefficient. The A-type AFM structure consists of *ab*-plane layers of spins ferromagnetically aligned along the c axis with AFM alignment of the spins in adjacent layers along this axis. The positive Weiss temperatures obtained from Curie-Weiss fits to the $\chi(T > T_N)$ data indicate that the dominant magnetic interactions are ferromagnetic (FM) for all x. A magnetic phase boundary is inferred to be present between $x = 0.14$ and $x = 0.17$ from a discontinuity in the x dependencies of the effective moment and Weiss temperature in the Curie-Weiss fits. FM fluctuations that strongly increase with increasing x are also revealed from the $\chi(T)$ data. The magnetic ground state for $x \geqslant 0.17$ is a spin glass as indicated by hysteresis in $\chi(T)$ between field-cooled and zero-field-cooled measurements and from the relaxation of M in a small field that exhibits a stretched-exponential time dependence. The spin glass has a small FM component to the ordering and is hence inferred to be comprised of small FM clusters. The competing AFM and FM interactions along with crystallographic disorder associated with Ir substitution are inferred to be responsible for the development of a FM cluster-glass phase. A logarithmic T dependence of C_p at low T for $x = 0.14$ is consistent with the presence of significant FM quantum fluctuations. This composition is near the $T = 0$ boundary at $x \approx 0.16$ between the A-type AFM phase containing ferromagnetically-aligned layers of spins and the FM cluster-glass phase.

DOI: 10.1103/PhysRevB.102.024410

I. INTRODUCTION

Since the discovery of high-T_c superconductivity (SC) in doped iron arsenides AFe_2As_2 (A = Ca, Sr, Ba, Eu), the interplay between magnetism and SC in these materials opened up new research areas [1–10]. Ternary arsenide compounds having the general formula AM_2As_2 (M = transition metal) commonly crystallize in the layered body-centered-tetragonal $ThCr_2Si_2$-type crystal structure. Here M_2As_2 layers are comprised of edge-sharing MAs_4 tetrahedra and the A atoms occupy layers between the M_2As_2 layers. Depending on the ratio c/a of the tetragonal c and a lattice parameters, a compound can crystallize in either the collapsed-tetragonal (cT) or uncollapsed-tetragonal (ucT) version of the structure or in the crossover regime [11–14]. Electron and/or hole doping in the three different atomic sites have been reported to introduce superconducting and/or magnetic phenomena in these materials. Fe-based arsenide compounds have been extensively studied after the discovery of SC at $T_c = 38$ K in K-doped $BaFe_2As_2$ in 2008 [1]. Both hole doping and electron doping subsequently resulted in the observation of SC in the AFe_2As_2 (A = Sr, Ca, and Eu) systems [15–18]. In these systems, SC is realized by suppressing the long-range antiferromagnetic (AFM) order of the parent compounds through chemical substitution or by the application of pressure. Later it was found that the suppression of long-range AFM order while preserving strong dynamic short-range AFM correlations was required for SC to appear, indicating that AFM fluctuations are required for the appearance of SC in the iron arsenides [2–4,6–10]. The self-doped alkali-metal compounds KFe_2As_2 ($T_c = 3.8$ K), $RbFe_2As_2$ ($T_c = 2.6$ K), and $CsFe_2As_2$ ($T_c = 2.6$ K) also exhibit SC [15,19,20]. These discoveries sparked interest in studying other transition-element-based analogs of this family of materials.

Metallic $ThCr_2Si_2$-type CoAs-based compounds exist but so far do not exhibit SC. However, these materials have attracted significant interest due to their peculiar itinerant magnetic behavior arising from their electronic structure and sensitivity to chemical substitution. For example, metallic $BaCo_2As_2$ has an ucT structure and does not exhibit long-range magnetic ordering down to a temperature $T = 1.8$ K [21,22]. However, crystals of this compound have a rather large magnetic susceptibility χ with a broad maximum followed by a weak low-temperature upturn [21]. A large exchange-enhanced density of states at the Fermi energy $\mathcal{D}(E_F) \approx 18$ states/eV f.u. was estimated for the material

from low-T heat-capacity data, where f.u. stands for formula unit [22]. In the initial report, it was argued that long-range ferromagnetic (FM) ordering is suppressed by quantum fluctuations [21], although a subsequent study [22] showed that the properties of $BaCo_2As_2$ are not very sensitive to chemical doping.

On the other hand, $SrCo_2As_2$ crystallizes in the ucT structure and $CaCo_{2-y}As_2$ crystallizes in the cT structure [14,16,23–25]. Metallic $SrCo_2As_2$ is a Stoner-enhanced paramagnet with no long-range magnetic ordering or SC at temperatures above 0.05 K [26]. Inelastic neutron-scattering measurements revealed the presence of stripe-type AFM fluctuations at the same wave vector as observed for the high-T_c parent compounds AFe_2As_2 [26,27]. However, in contrast to the AFe_2As_2 compounds, no obvious Fermi-surface nesting was observed at that wave vector for $SrCo_2As_2$ and, furthermore, FM fluctuations occur that evidently hinder the occurrence of SC [28,29]. FM fluctuations were also observed in FeAs-based superconductors, suggesting that the different T_c's observed in these materials may be at least partially explained by different levels of FM fluctuations in the compounds [30].

In contrast to $BaCo_2As_2$ and $SrCo_2As_2$, a detectable concentration of vacancies is observed on the Co sites in $CaCo_{2-y}As_2$ that undergoes A-type AFM ordering with propagation vector $\vec{\tau} = (0, 0, 1)$ at $T_N = 52-77$ K, depending on the crystal [25,31,32]. In this magnetic structure, the ordered moments on the Co sites within the *ab* plane are ferromagnetically aligned along the *c* axis with AFM alignment between adjacent planes. FM interactions dominate together with relatively weak AFM interactions between Co planes responsible for the A-type AFM ordering. Inelastic neutron-scattering experiments reveal the presence of strong magnetic frustration in the system within the J_1-J_2 Heisenberg model on a square lattice with the nearest-neighbor exchange interaction being FM [33]. This strong magnetic frustration establishes $CaCo_{2-y}As_2$ as a unique member of the ternary arsenide family.

Chemically-doped Co-based arsenides are of significant interest due to the interplay between the lattice, electronic, and magnetic degrees of freedom. For example, the K-doped compound $Ba_{0.94}K_{0.06}Co_2As_2$ shows weak FM behavior; however, the magnetic behavior of the composition $Ba_{0.78}K_{0.22}Co_2As_2$ is found to be quite similar to that observed for undoped $BaCo_2As_2$ [22]. This difference has been suggested to be due to different Co defect levels associated with the crystal growth.

It has also been discovered that the system $Ca_{1-x}Sr_xCo_{2-y}As_2$ exhibits a composition-induced crossover in the magnetic anisotropy [34,35]. In the region $0 \leqslant x \lesssim 0.2$, the compounds order in the A-type AFM structure where the moments are aligned along the *c* axis as in $CaCo_{2-y}As_2$. At temperature $T = 5$ K and $0.2 \lesssim x \lesssim 0.3$, the moments are still aligned along the *c* axis but with a $++--$ configuration with propagation vector $\vec{\tau} = (0, 0, 1/2)$ [36]. For compositions $0.3 \lesssim x \lesssim 0.5$, the ordered moments also have the propagation vector $\vec{\tau} = (0, 0, 1/2)$ but with the moments now aligned in the *ab* plane with ether a $++--$ ordering or a 90° helix AFM configuration along the *c* axis [36]. Finally, for $x \gtrsim 0.5$, the material exhibits no magnetic transitions above 2 K. It was concluded from theoretical modeling of the structures obtained from the neutron-diffraction measurements that single-ion magnetic anisotropy and frustration of AFM nearest- and next-nearest-layer exchange interactions are all composition dependent in $Ca_{1-x}Sr_xCo_{2-y}As_2$ [36]. The composition $x = 0.33$ exhibits a temperature-induced transition between moment alignments in the *ab* plane and along the *c* axis [35].

Recently, non-Fermi-liquid types of behavior associated with a composition-induced magnetic quantum-critical point in $Sr(Co_{1-x}Ni_x)_2As_2$ crystals near $x = 0.3$ has been reported [37]. In addition, crystals of $Sr(Co_{1-x}Ni_x)_2As_2$ with $0 < x < 0.3$ exhibit *c*-axis helical or spin-density-wave AFM ordering [37–39], which is quite unusual in itinerant antiferromagnets. A small amount (2.5%) of La doping has been reported to cause FM ordering in $Sr_{1-x}La_xCo_2As_2$ [40,41]. In $CaCo_{2-y}As_2$, the A-type AFM order was found to be smoothly suppressed by Fe doping on the Co site [42].

The above studies illustrate the impact of chemical substitution/doping on the physical properties exhibited by the Co122 systems. Since the alkaline-earth Co-As systems exhibit itinerant magnetism that originates from the properties of band electrons near the Fermi surface, the magnetic properties strongly depend on the electronic effects of substituting/doping by different elements. Most such studies have been carried out using 3*d*- and 4*d*-transition metal substitutions on the Co sites, and the effect of substituting 5*d* atoms for Co has not been emphasized. Moreover, the high atomic number of 5*d* elements is expected to significantly alter the magnetic interaction in those systems due to the strong spin-orbit coupling associated with such atoms. Spin-orbit coupling has been considered to be an important tool to tune the superconducting and magnetic properties of different systems [43–48]. Thus, it is interesting to examine whether 5*d*-element substitutions on the Co site can reveal novel properties and ground states.

In this paper, we report the influence of Ir (5*d*) substitutions for Co in $CaCo_{1.86}As_2$ on the crystallographic, magnetic, and thermal properties. Although all the $Ca(Co_{1-x}Ir_x)_{2-y}As_2$ compounds are found to crystallize in the cT structure as in the parent compound, the Ir substitutions significantly alter the magnetic interactions in these systems. A composition-induced crossover from the A-type AFM state to a magnetically disordered FM cluster-glass state is observed. The $x = 0.14$ composition exhibits signatures of FM quantum fluctuations with a concomitant significant increase in the electronic Sommerfeld coefficient.

The experimental details are given in Sec. II. The crystallography results are presented in Sec. III, magnetization and magnetic susceptibility data in Sec. IV, a study of the magnetism of the glassy state in Sec. V, and the heat-capacity measurements in Sec. VI. A summary of the results is given in Sec. VII.

II. EXPERIMENTAL DETAILS

Single crystals of $Ca(Co_{1-x}Ir_x)_{2-y}As_2$ with $x = 0$, 0.033, 0.065, 0.10, 0.14, 0.17, 0.25, and 0.35 were grown out of (Co,Ir)As self flux using the high-temperature solution-growth technique. The high-purity starting materials Ca (99.999%, Alfa Aesar), Co (99.998%, Alfa Aesar),

TABLE I. Room-temperature crystallographic data for $Ca(Co_{1-x}Ir_x)_{2-y}As_2$ ($0 \leqslant x \leqslant 0.35$, $0.10 \leqslant y \leqslant 0.14$) single crystals. The labeled compositions were estimated from EDS analyses. Also listed are the tetragonal lattice parameters a and c, the unit cell volume V_{cell}, the c/a ratio, and the fractional c-axis position of the As site (z_{As}) obtained from single-crystal XRD data.

Compound	a (Å)	c (Å)	V_{cell} (Å^3)	c/a	z_{As}
$CaCo_{1.86(2)}As_2$	3.9837(4)	10.2733(4)	163.04(9)	2.5788(6)	0.3672(4)
$Ca(Co_{0.967(3)}Ir_{0.033(3)})_{1.86(2)}As_2$	3.988(1)	10.268(7)	163.3(1)	2.575(8)	0.3665(1)
$Ca(Co_{0.935(5)}Ir_{0.065(5)})_{1.86(2)}As_2$	3.990(2)	10.268(7)	163.5(2)	2.573(9)	0.3664(2)
$Ca(Co_{0.90(1)}Ir_{0.10(1)})_{1.86(2)}As_2$	3.996(2)	10.274(5)	164.1(2)	2.571(7)	0.3662(2)
$Ca(Co_{0.86(1)}Ir_{0.14(1)})_{1.87(2)}As_2$	3.996(2)	10.294(5)	164.3(2)	2.577(7)	0.3672(2)
$Ca(Co_{0.83(1)}Ir_{0.17(1)})_{1.87(2)}As_2$	4.005(1)	10.315(3)	165.5(1)	2.575(4)	0.3677(2)
$Ca(Co_{0.75(2)}Ir_{0.25(2)})_{1.89(2)}As_2$	4.017(1)	10.305(3)	166.3(1)	2.565(4)	0.3681(2)
$Ca(Co_{0.65(4)}Ir_{0.35(4)})_{1.90(2)}As_2$	4.029(1)	10.326(3)	167.7(1)	2.562(4)	0.3684(2)

Ir (99.9999%, Ames Laboratory), and As (99.9999%, Alfa Aesar) were taken in the molar ratio Ca:Co:Ir:As = 1:4(1 − x):4x:4 and placed in an alumina crucible. The crucible was then sealed in a silica tube under ≈1/4 atm of Ar gas. Quartz wool was placed above the filled crucible to extract the flux during centrifugation. The assembly was preheated to 650 °C for 6 h and then heated to 1300 °C at 50 °C/h. The sample was kept at that temperature for 20 h for homogenization. Then the tube was cooled to 1180 °C at a rate of 6 °C/h and the single crystals were separated from the flux using a centrifuge. Shiny platelike single crystals of different sizes were obtained from the growths with the c axis perpendicular to the plate surfaces. However, the crystal size and homogeneity both decreased with increasing Ir substitution, so we could not obtain crystals with $x > 0.35$.

The phase homogeneity and the average composition of the $Ca(Co_{1-x}Ir_x)_{2-y}As_2$ crystals were determined using a scanning-electron microscope equipped with an energy-dispersive x-ray spectroscopy (EDS) attachment from JEOL. The chemical compositions were measured at many points on both surfaces of the platelike crystals to confirm their chemical homogeneity. The average compositions of the crystals used for different measurements are listed in Table I.

Single-crystal x-ray diffraction (XRD) measurements were performed at room temperature on a Bruker D8 Venture diffractometer operating at 50 kV and 1 mA equipped with a Photon 100 CMOS detector, a flat graphite monochromator, and a Mo Kα IμS microfocus source ($\lambda = 0.71073$ Å). The raw frame data were collected using the Bruker APEX3 program [49], while the frames were integrated with the Bruker SAINT software package [50] using a narrow-frame algorithm for integration of the data and were corrected for absorption effects using the multiscan method (SADABS) [51]. The atomic thermal factors were refined anisotropically. Initial models of the crystal structures were first obtained with the program SHELXT-2014 [52] and refined using the program SHELXL-2014 [53] within the APEX3 software package.

The $M(H, T)$ data were obtained using a Quantum Design, Inc., magnetic-properties measurement system SQUID magnetometer in the range $T = 1.8$ to 300 K with magnetic fields up to 5.5 T (1 T $\equiv 10^4$ Oe). The heat-capacity $C_p(H, T)$ measurements were performed using the relaxation technique in a Quantum Design, Inc., physical-properties measurement system in the ranges $T = 1.8-300$ K and $H = 0-9$ T.

III. CRYSTALLOGRAPHY

The room-temperature single-crystal XRD measurements demonstrated that the $Ca(Co_{1-x}Ir_x)_{2-y}As_2$ ($0 \leqslant x \leqslant 0.35$) crystals form in the body-centered tetragonal $ThCr_2Si_2$-type crystal structure (space group $I4/mmm$) shown in Fig. 1. The crystallographic parameters are listed in Table I. Generally, when the c/a ratio is less than 2.67, the system is considered to form with a cT crystal structure [14]. The c/a values for the present crystals are well below that value indicating that all the Ir-substituted compositions in our study form in a cT structure as does the undoped $CaCo_{2-y}As_2$ parent compound. The EDS results reveal that the vacancy concentration on the Co site changes from 7(1)% in the parent $CaCo_{1.86(2)}As_2$ compound to 5(1)% with 35% Ir substitution. As a single-crystal XRD refinement does not allow for simultaneous refinement of the fraction Co/Ir and total occupation of the position, only the total occupancies were refined based on the Co/Ir ratio taken from the EDS data. The variation in the Ir content

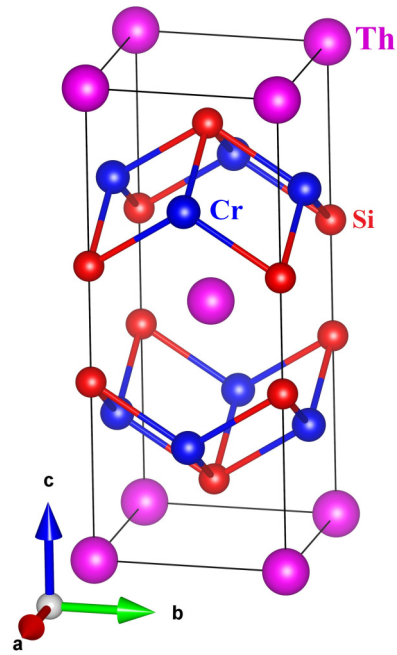

FIG. 1. Unit cell of the body-centered tetragonal $ThCr_2Si_2$ crystal structure. The figure was drawn using VESTA [54].

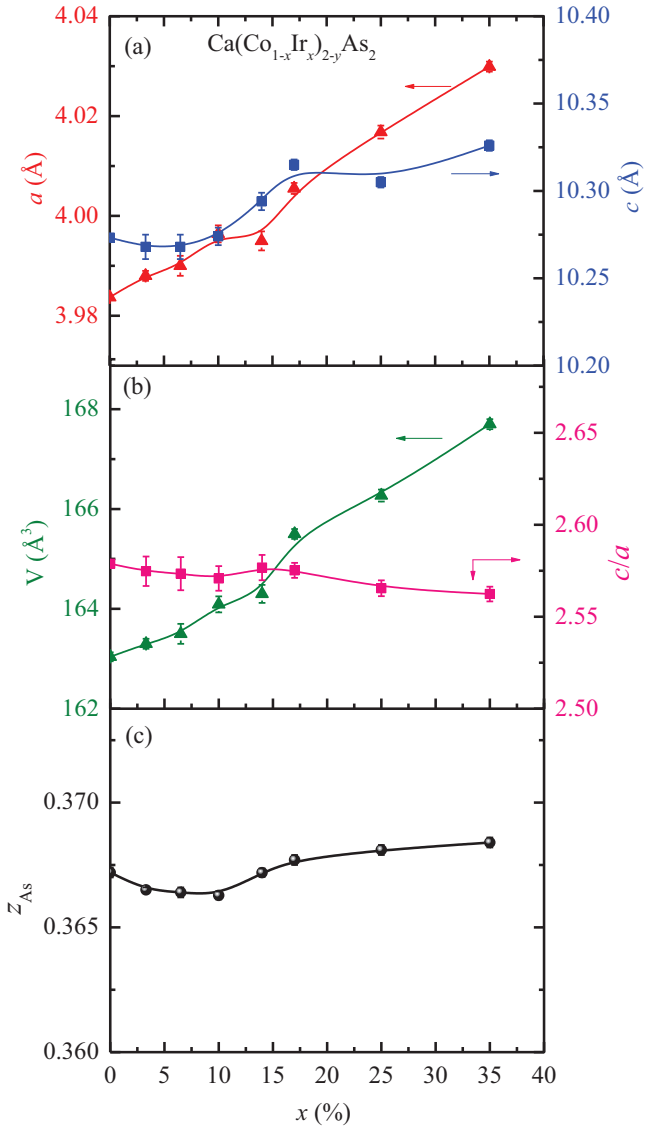

FIG. 2. Crystallographic parameters: (a) tetragonal lattice parameters a and c, (b) unit cell volume V and c/a ratio, and (c) c-axis As position parameter (z_{As}) of $Ca(Co_{1-x}Ir_x)_{2-y}As_2$ compounds as a function of Ir substitution x. The lines are guides to the eye.

within the crystals as reflected in the compositional error bars was found to be small for low Ir substitution levels. However, the inhomogeneity increases for 35% Ir-substituted crystals. The crystallographic parameters are plotted versus Ir concentration x in Figs. 2(a)–2(c). Both lattice parameters a and c are found to increase nonlinearly with increasing Ir substitution giving rise also to a nonlinear increase of the unit cell volume V_{cell} with increasing x.

IV. MAGNETIC SUSCEPTIBILITY

The temperature dependence of the magnetization for $Ca(Co_{1-x}Ir_x)_{2-y}As_2$ crystals was measured under zero-field-cooled (ZFC) and field-cooled (FC) protocols in a magnetic field $H = 0.1$ T applied in the ab plane ($H \parallel ab$) and along the c axis ($H \parallel c$). Figures 3(a)–3(h) show the temperature dependence of the magnetic susceptibility $\chi \equiv M/H$ for all

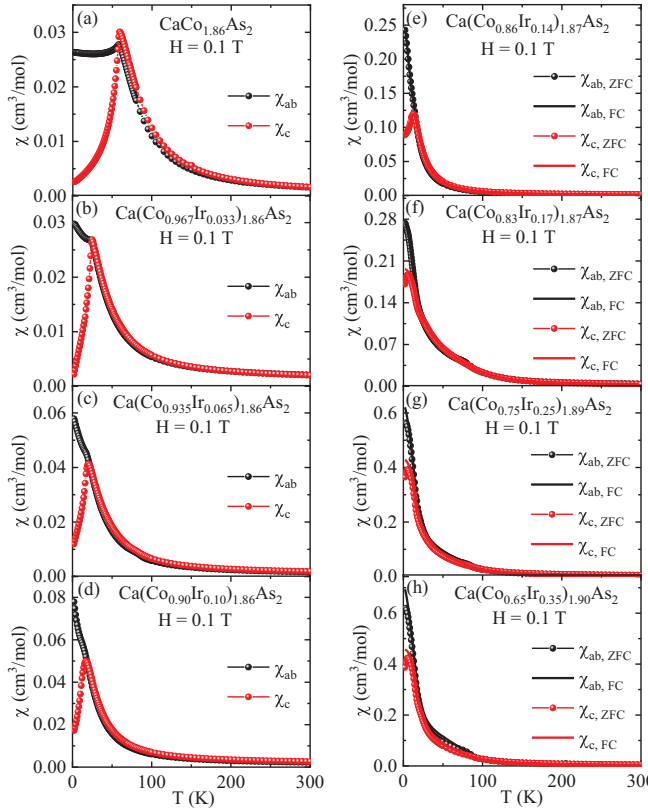

FIG. 3. Magnetic susceptibility ($\chi = M/H$) as a function of temperature T for $Ca(Co_{1-x}Ir_x)_{2-y}As_2$ single crystals in a magnetic field $H = 0.1$ T applied in the ab plane (χ_{ab}) and along the c axis (χ_c). Note the strong increase in the ordinate scale with increasing x and the associated increase in the temperature dependence of χ_{ab} below the cusp temperature for χ_c.

eight $Ca(Co_{1-x}Ir_x)_{2-y}As_2$ crystals. Evidence for some type of magnetic ordering is seen for each of the crystals. The details on the possible nature of the magnetic ground states are as follows.

A. Antiferromagnetic ordering temperature T_N for $0 \leqslant x \leqslant 0.14$

The parent compound $CaCo_{1.86(2)}As_2$ orders in an A-type AFM structure at $T_N = 52(1)$ K as reported earlier [25], where $\chi_c(T \to 0) = 0$ and χ_{ab} is nearly independent of T below T_N. These are the characteristic signatures of a c-axis collinear antiferromagnet. In this magnetic structure of $CaCo_{1.86(2)}As_2$, as noted above the ordered moments within an ab plane are aligned ferromagnetically along the c axis with the moments in adjacent layers along the c axis aligned antiferromagnetically. Thus, $\chi(T)$ below T_N is anisotropic with the c axis as the easy axis.

Figure 4(a) shows expanded plots of χ_{ab} and χ_c versus T for $Ca(Co_{1-x}Ir_x)_{2-y}As_2$ crystals with $x = 0$ to $x = 0.14$. For antiferromagnets with an easy c axis as in $CaCo_{2-y}As_2$, the Néel temperature is the temperature of the peak in the derivative $d(\chi_c T)/dT$ [55]. Plots of $d(\chi_c T)/dT$ versus T are shown in Fig. 4(b) where the T_N values obtained from the temperatures of the peaks are listed in Table II. The T_N decreases rapidly to 23(1) K for 3.3% Ir substitution.

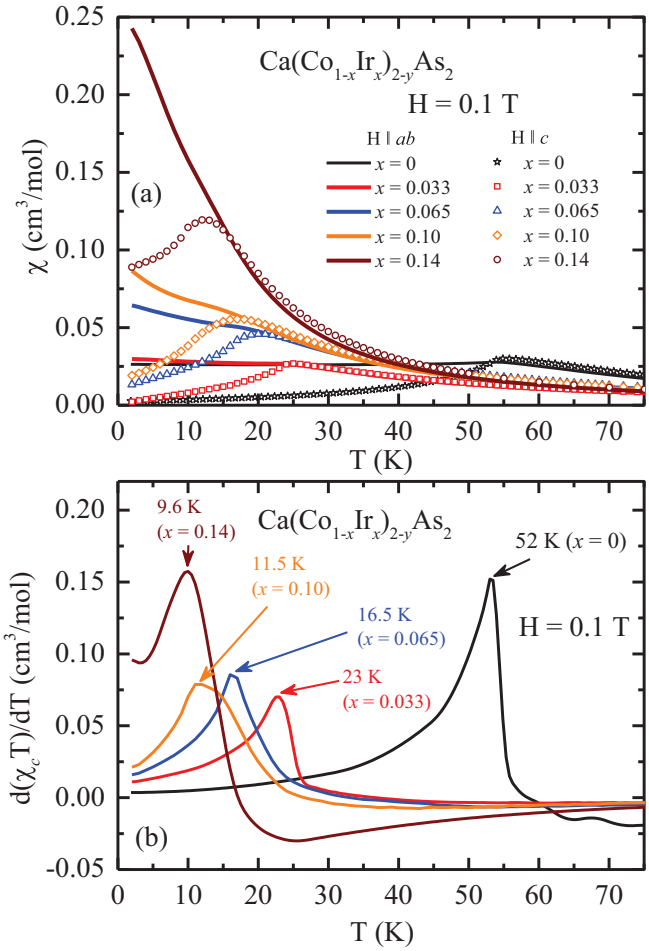

FIG. 4. (a) Expanded plots of the zero-field-cooled magnetic susceptibilities $\chi_{ab}(T)$ and $\chi_c(T)$ with $H = 0.1$ T for $Ca(Co_{1-x}Ir_x)_{2-y}As_2$ crystals with compositions $x = 0$ to 0.14. (b) Temperature derivative $d(\chi_c T)/dT$ versus T obtained for the crystals, where the temperatures of the peaks are identified as the Néel temperatures versus Ir concentration x.

Moreover, with increasing x, the magnitudes of both χ_{ab} and χ_c increase significantly below T_N, suggesting an increase in FM fluctuations. Interestingly, though the χ_c suggests an AFM ordering below 9.6 K for $x = 0.14(1)$, χ_{ab} does not show any peak/cusp/inflection at T_N and increases monotonically for temperatures down to 2 K.

B. Magnetic susceptibility in the paramagnetic state

The $\chi(T)$ data in the paramagnetic (PM) state at $T > T_N$ are analyzed in terms of local moments using the modified Curie-Weiss law

$$\chi_\alpha(T) = \chi_0 + \frac{C_\alpha}{T - \theta_{p\alpha}} \qquad (\alpha = ab,\ c), \tag{1}$$

where χ_0 is an isotropic temperature-independent term that contains the diamagnetic contributions from the atomic cores and the conduction-carrier orbital Landau susceptibilities, together with the paramagnetic contribution from the Pauli spin susceptibility of the conduction carriers. The Curie constant

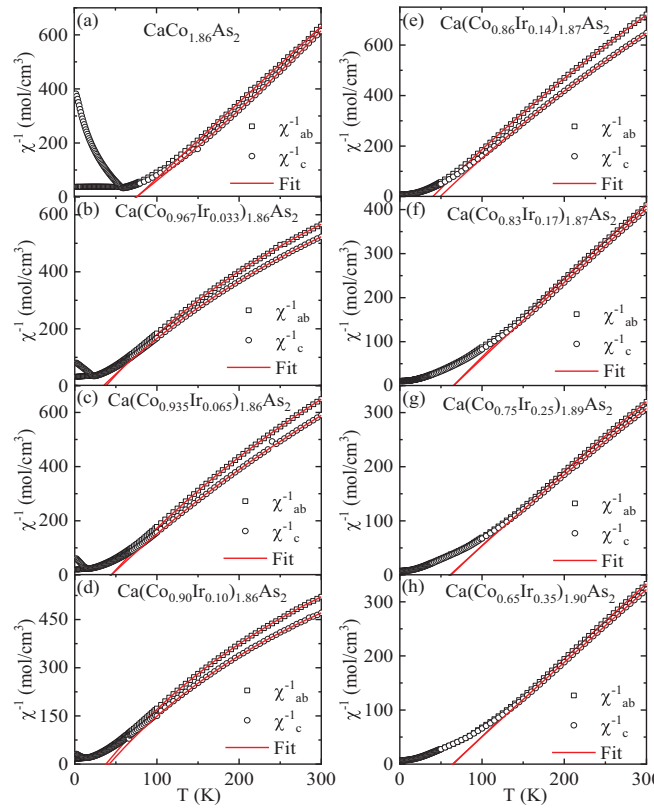

FIG. 5. The temperature dependence of zero-field-cooled (ZFC) inverse magnetic susceptibility in magnetic field $H = 1$ T applied along both the ab plane and the c axis. The red solid lines are fits by the modified Curie-Weiss law in Eq. (1) between 150 and 300 K. The red solid curves at lower temperatures are extrapolations of the fits.

per mole of formula units (f.u.) is given by

$$C_\alpha = \frac{N_A g_\alpha{}^2 S(S+1)\mu_B^2}{3k_B} = \frac{N_A \mu_{\mathrm{eff}\alpha}^2}{3k_B} \qquad (\alpha = ab,\ c), \tag{2}$$

where N_A is Avogadro's number, g_α is the spectroscopic splitting factor (g factor), S is the spin angular-momentum quantum number, k_B is Boltzmann's constant, and μ_{eff} is the effective moment of a spin in units of Bohr magnetons μ_B. Inserting the Gaussian cgs values of the fundamental constants into Eq. (2), the Curie constant per mole of spins is expressed as

$$C_\alpha(\mathrm{cm^3\,K/mol}) \approx \frac{\mu_{\mathrm{eff}}^2}{8}\,(\mu_B/\mathrm{f.u.}). \tag{3}$$

Hence

$$\mu_{\mathrm{eff}\alpha}\,(\mu_B/\mathrm{f.u.}) \approx \sqrt{8C_\alpha}. \tag{4}$$

The anisotropic inverse susceptibilities of the $Ca(Co_{1-x}Ir_x)_{2-y}As_2$ crystals are plotted versus temperature in Fig. 5. The fitted parameters for the $\chi^{-1}(T)$ data in Fig. 5 obtained over the temperature range 150 K to 300 K using the modified Curie-Weiss law are listed in Table II. The fits are shown as the solid red curves in Fig. 5. The effective moment μ_{eff} and Weiss temperature θ_p are plotted versus x in Figs. 6(a) and 6(b), respectively.

TABLE II. Parameters obtained from modified Curie-Weiss fits to $\chi^{-1}(T)$ data between 150 and 300 K for $Ca(Co_{1-x}Ir_x)_{2-y}As_2$ by using Eq. (1). Shown are the T-independent contributions to the susceptibility χ_0, Curie constant per mol C_α in $\alpha = ab, c$ directions, Weiss temperature $\theta_{p\alpha}$, and effective moment per formula unit (f.u.) $\mu_{eff\alpha}(\mu_B/f.u.) = \sqrt{8C_\alpha}$ calculated from Eq. (4). Also included are the Néel temperatures T_N obtained from the temperatures of the cusps in $d(\chi_c T)/dT$ in Fig. 4(b), the *ab*-plane spin-flop fields H_{SF} at $T = 2$ K, and the blocking temperatures T_B.

Compound	Field Orientation	χ_0 (10^{-4} $\frac{cm^3}{mol}$)	C_α ($\frac{cm^3 K}{mol}$)	$\mu_{eff\alpha}$ ($\frac{\mu_B}{f.u.}$)	$\theta_{p\alpha}$ (K)	T_N (K)	H_{SF} (kOe)	T_B (K)
$CaCo_{1.86}As_2$	$H \parallel ab$	0.03(2)	0.354(7)	1.68(2)	76(1)	53	35.0(5)	
	$H \parallel c$	−0.2(2)	0.416(3)	1.82(1)	75(1)			
$Ca(Co_{0.967}Ir_{0.033})_{1.86}As_2$	$H \parallel ab$	5.8(2)	0.308(8)	1.57(2)	38(2)	23	22.5(5)	
	$H \parallel c$	5.72(6)	0.355(2)	1.67(1)	34.8(5)			
$Ca(Co_{0.935}Ir_{0.065})_{1.86}As_2$	$H \parallel ab$	3.58(3)	0.316(4)	1.59(1)	44.2(2)	16.5	17.5(1)	
	$H \parallel c$	3.39(5)	0.357(4)	1.69(1)	44.5(5)			
$Ca(Co_{0.90}Ir_{0.10})_{1.86}As_2$	$H \parallel ab$	6.9(1)	0.320(3)	1.60(1)	38(1)	11.5	15.0(2)	
	$H \parallel c$	7.9(1)	0.361(5)	1.70(1)	42(1)			
$Ca(Co_{0.86}Ir_{0.14})_{1.87}As_2$	$H \parallel ab$	1.9(2)	0.310(7)	1.57(2)	40(2)	9.6	5.0(1)	
	$H \parallel c$	2.61(5)	0.322(2)	1.60(1)	49(1)			
$Ca(Co_{0.83}Ir_{0.17})_{1.87}As_2$	$H \parallel ab$	1.8(2)	0.529(8)	2.06(2)	65(1)			6.1
	$H \parallel c$	1.1(2)	0.559(7)	2.11(1)	65.4(9)			
$Ca(Co_{0.75}Ir_{0.25})_{1.89}As_2$	$H \parallel ab$	2.4(2)	0.686(6)	2.34(1)	62.3(7)			5.5
	$H \parallel c$	2.5(4)	0.716(12)	2.39(2)	61(1)			
$Ca(Co_{0.65}Ir_{0.35})_{1.90}As_2$	$H \parallel ab$	1.0(2)	0.681(7)	2.35(1)	65(1)			4.5
	$H \parallel c$	0.8(2)	0.715(11)	2.39(2)	64(1)			

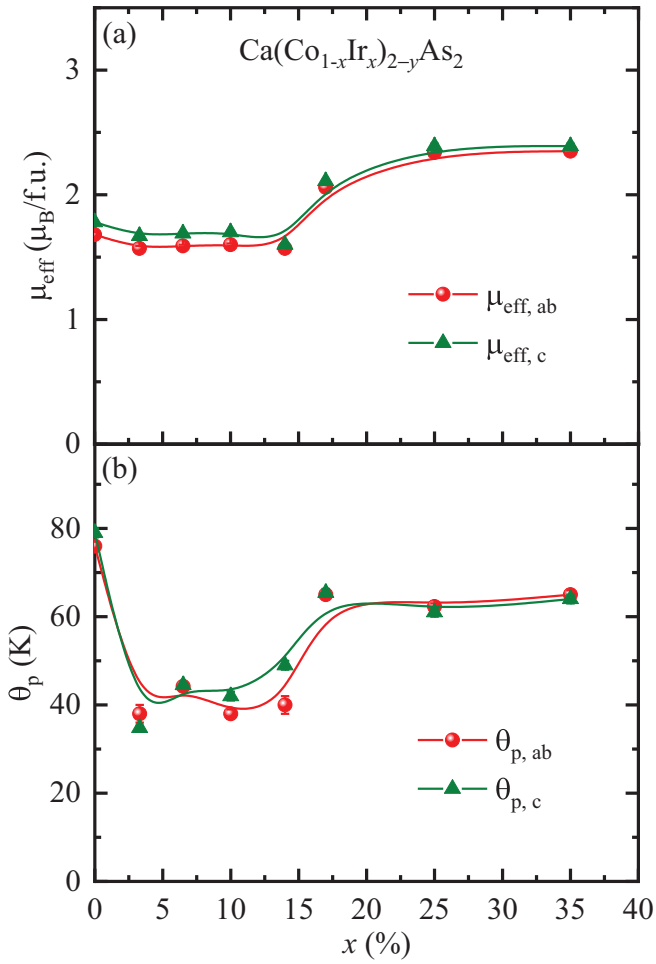

FIG. 6. Effective magnetic moment μ_{eff} and the Weiss temperature θ_p as a function of x. The lines are guides to the eye.

For spins S with $g = 2$, the isotropic Curie constant in units of cm^3 K/mol spins is

$$C = 0.5002S(S+1). \quad (5)$$

The $Ca(Co_{1-x}Ir_x)_{2-y}As_2$ system has approximately 1.9 transition-metal atoms per formula unit and assuming that the Co/Ir atoms carry a local moment, Eq. (5) gives

$$C_{mol} \approx 0.95S(S+1) \quad (6)$$

per mole of $Ca(Co_{1-x}Ir_x)_{2-y}As_2$ formula units. Thus if $S = 1/2$ with $g = 2$, we expect $C_{mol} \approx 0.74\,cm^3$ K/mol, whereas $S = 1$ gives $C_{mol} \approx 1.80\,cm^3$ K/mol. From Table II, the Curie constants are in the range 0.31–0.36 cm^3 K/mol for $0 \leqslant x \leqslant 0.14$ and 0.53–0.72 cm^3 K/mol for $0.17 \leqslant x \leqslant 0.35$. Thus there is a significant change in the magnetic character of $Ca(Co_{1-x}Ir_x)_{2-y}As_2$ between the composition ranges $0 \leqslant x \leqslant 0.14$ and $0.17 \leqslant x \leqslant 0.35$, suggesting the presence of a magnetic phase boundary at $x \approx 0.15$. In addition, the large discrepancy between the measured values for $x \leqslant 0.14$ and the values obtained from Eq. (6) suggests that the magnetism is itinerant for these compositions as previously deduced for $x = 0$ (see, e.g., Ref. [33]). On the other hand, the larger values of C_{mol} for the range $0.17 \leqslant x \leqslant 0.35$ compared with those at lower x values suggests an increased local-moment character for $x \geqslant 0.17$.

C. Magnetization versus applied magnetic field isotherms

To further clarify the magnetic ground states in $Ca(Co_{1-x}Ir_x)_{2-y}As_2$, $M(H)$ isotherms were measured at different temperatures in the field range 0–5.5 T, as shown in Figs. 7(a)–7(g) for $H \parallel ab$ and Figs. 7(h)–7(n) for $H \parallel c$. The $M(H)$ behavior in both field directions is nonlinear up to a much higher temperature than their

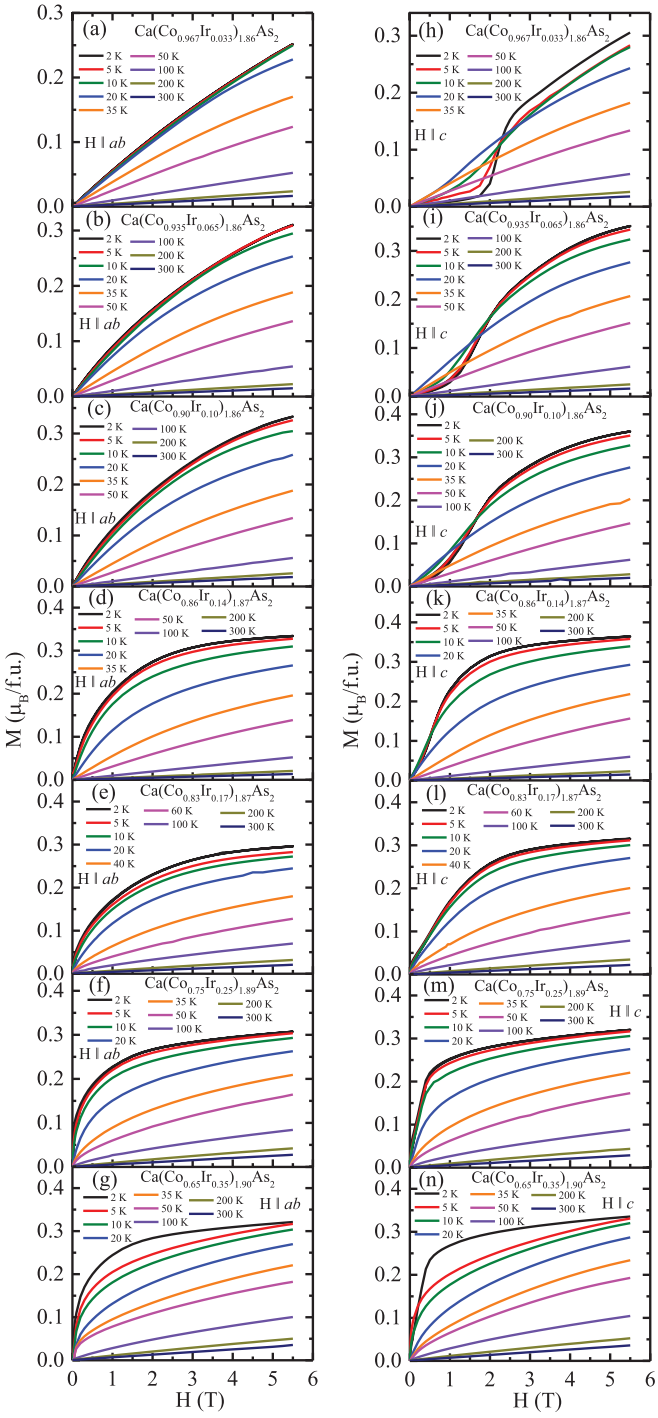

FIG. 7. (a)–(g) Magnetic field dependence of in-plane isothermal magnetization (M_{ab}) measured at different temperatures for the $Ca(Co_{1-x}Ir_x)_{2-y}As_2$ crystals when $H \parallel ab$. (h)–(n) Out-of-plane isothermal magnetization (M_c) versus H measured at different temperatures for $H \parallel c$. Here the data have been shown for the crystals with $x > 0$, whereas the data for $x = 0$ are given in Ref. [25].

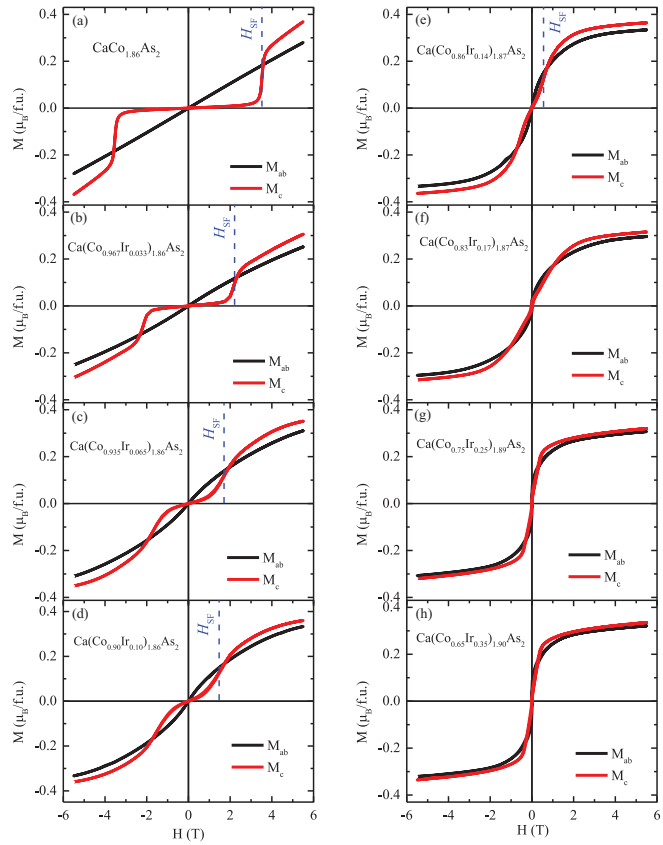

FIG. 8. Magnetization M versus applied magnetic field H measured at $T = 2$ K for the $Ca(Co_{1-x}Ir_x)_{2-y}As_2$ crystals in the ab plane (M_{ab}) and along c axis (M_c) over the full field range of the measurements. The $M_c(H)$ data for $x = 0 - 0.14$ in (a)–(e) exhibit spin-flop transitions from the c axis to the ab plane, whereas the data for $x = 0.17-0.35$ in (f)–(h) suggest the onset of an ordered FM component in the ab plane. The spin-flop fields H_{SF} in panels (a)–(e) are the midpoint fields of the spin-flop transitions and are indicated by vertical dashed lines.

characteristic temperature T_N or T_B due to the presence of short-range magnetic interactions. Figures 8(a)–8(h) show $M(H)$ isotherms at $T = 2$ K for different compositions with both field directions. Here $M_{ab}(H)$ for $x = 0$ increases linearly with H whereas $M_c(H)$ clearly exhibits a spin-flop (SF) transition at $H_{SF} = 3.5$ T, similar to the results reported earlier [25]. However, the SF transition field rapidly decreases to $H_{SF} = 2.15(5)$ T for $x = 0.033$, while retaining a linear $M_{ab}(H)$ behavior up to $H = 5.5$ T. For both crystals, no tendency towards saturation was observed in either $M_{ab}(H)$ or $M_c(H)$ isotherms in the field region studied. The H_{SF} decreases further with increasing x and becomes negligible for $x = 0.14$. The jump in $M_c(H)$ at H_{SF} also broadens with increasing x.

The magnetizations $M_{ab}(H)$ and $M_c(H)$ for $x = 0.065$ and 0.10 exhibit a saturation tendency at higher fields, suggesting a reduction of AFM interactions with increasing Ir concentration. The magnetic saturation tendency is observed at much lower H for $x = 0.14$ and at the highest applied field the magnetization almost saturates to the saturation magnetizations $M_{ab}^{sat} = 0.33\,\mu_B$/f.u. and $M_c^{sat} = 0.36\,\mu_B$/f.u. Thus the saturation moment per Co/Ir atom is only about 0.16 and 0.18 μ_B for these two compositions. The compounds with $x \geqslant 0.17$ do not show a SF transition. Instead, $M_{ab}(H)$ and $M_c(H)$ almost saturate for $H \gtrsim 3.7$ T.

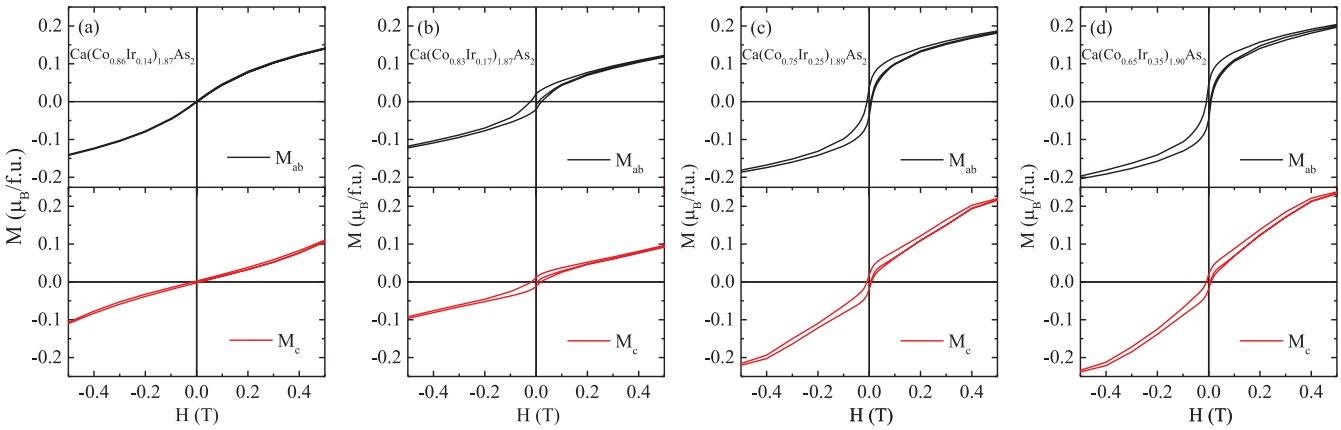

FIG. 9. Low field region of magnetic hysteresis behavior measured at $T = 2$ K in the *ab* plane (upper panel) and along *c* axis (lower panel) for the $Ca(Co_{1-x}Ir_x)_{2-y}As_2$ crystals with (a) $x = 0.14$, (b) $x = 0.17$, (c) $x = 0.25$, and (d) $x = 0.35$.

No magnetic hysteresis is observed in $M(H)$ for $x \leqslant 0.14$ as shown in Fig. 9(a). However, the more Ir-rich compounds exhibit low-temperature magnetic hysteresis with finite coercive fields H_{cf} signifying a FM volume fraction in these crystals as depicted in Figs. 9(b)–9(d) for both field directions. The remanent magnetization (M_{rem}) and H_{cf} of the $Ca(Co_{1-x}Ir_x)_{2-y}As_2$ crystals with $x = 0.17$, 0.25, and 0.35 are listed in Table III. The H_{cf} is maximum for $x = 0.17$, whereas it is about a factor of two smaller for $x = 0.25$ and 0.35. On the other hand, the M_{rem} values initially increase with increasing x, where M_{rem} in the *ab* plane is about a factor of two larger than along the *c* axis. This observation correlates with the magnetic susceptibility data in Fig. 3 where the *ab*-plane FM fluctuations are generally stronger than along the *c* axis.

The *c*-axis spin-flop transition field H_{SF} for $x = 0$–0.14 and the approximate spherically-averaged saturation moment $M_{sat,ave}$ for the $Ca(Co_{1-x}Ir_x)_{2-y}As_2$ crystals with $x = 0.14$ to 0.35 are summarized in Fig. 10.

V. MAGNETISM OF THE GLASSY STATE FOR $0.17 \leqslant x \leqslant 0.35$

Figure 11 depicts $\chi_{ab}(T)$ and $\chi_c(T)$ for $x = 0.14$, 0.17, 0.25, and 0.35 measured in $H = 0.1$ T, each under both ZFC and FC conditions. The data for the AFM composition $x = 0.14$ show no significant hysteresis between the FC and ZFC curves of the respective $\chi_{ab}(T)$ and $\chi_c(T)$ measurements. On the other hand, for the compositions $x = 0.17$, 0.25, and 0.35, which do exhibit hysteresis, the χ_c data for each x exhibit a broad maximum at a temperature denoting the blocking temperature T_B as listed in Table II, and χ_{ab} shows a FM-like saturation tendency below T_B. The hysteretic behavior of the $x = 0.17$, 0.25, and 0.35 compounds of the respective $\chi_{ab}(T)$ and $\chi_c(T)$ measurements is similar to the corresponding behavior for different glassy systems consisting of FM clusters [56–60]. In a spin-glass system spin freezing occurs below a blocking temperature T_B (often called T_f). Although the measurement of T_B is best estimated through ac magnetic susceptibility measurements, the T_B found from that measurement is the same temperature as the temperature of the maximum in the ZFC dc magnetic susceptibility measurement [61,62]. Thus, the data in Fig. 11 for $x = 0.17$, 0.25, and 0.35 are consistent with formation of FM clusters in these crystals.

A magnetic glassy state is metastable and found to exhibit a time-dependent relaxation behavior [61,63,64]. Magnetic relaxation dynamics can be studied in different ways. In

TABLE III. Remanent magnetization (M_{rem}) and coercive field (H_{cf}) of $Ca(Co_{1-x}Ir_x)_{2-y}As_2$ compounds with $x = 0.17$, 0.25, and 0.35.

Crystal Composition	H direction	M_{rem} (μ_B/f.u.)	H_{cf} (Oe)
$Ca(Co_{0.83}Ir_{0.17})_{1.87}As_2$	$H \parallel ab$	0.019(2)	220(2)
	$H \parallel c$	0.012(2)	190(2)
$Ca(Co_{0.75}Ir_{0.25})_{1.89}As_2$	$H \parallel ab$	0.038(1)	87(1)
	$H \parallel c$	0.018(1)	88(1)
$Ca(Co_{0.65}Ir_{0.35})_{1.90}As_2$	$H \parallel ab$	0.047(1)	90(2)
	$H \parallel c$	0.019(1)	92(2)

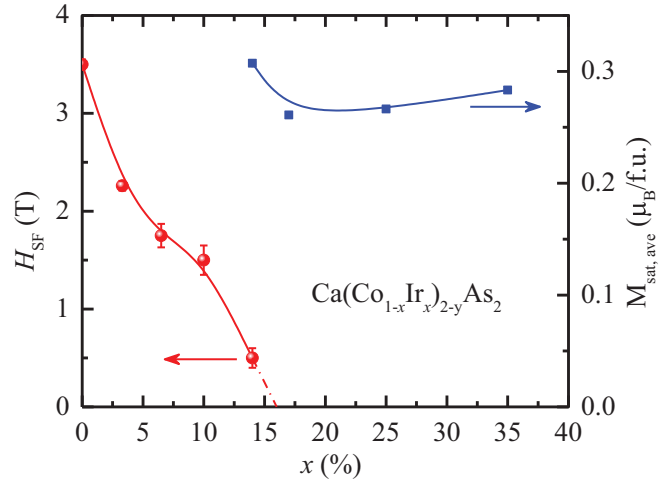

FIG. 10. Composition dependence of spin-flop field H_{SF} and spherically-averaged saturation moment ($M_{sat,ave}$) from Fig. 8 for $Ca(Co_{1-x}Ir_x)_{2-y}As_2$ crystals with an A-type AFM ground state. The lines are guides to the eye. According to the extrapolated $H_{SF}(x)$ data, the A-type AFM phase boundary is at $x \approx 0.16$.

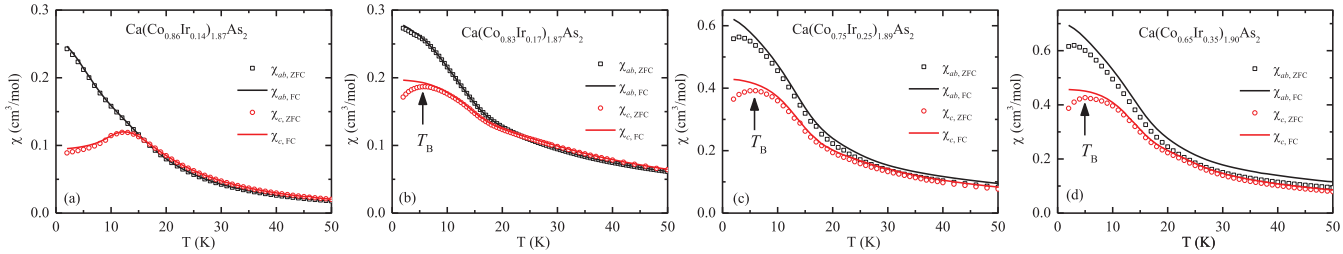

FIG. 11. Expanded plots at low temperatures of the magnetic susceptibilities $\chi_{ab}(T)$ and $\chi_c(T)$ under ZFC and FC conditions with $H = 0.1$ T for $Ca(Co_{1-x}Ir_x)_{2-y}As_2$ crystals with compositions $x = 0.14$ to 0.35. The blocking temperatures T_B for $x = 0.17$, 0.25, and 0.35 are indicated by vertical arrows.

the present work, the crystals were cooled to 2 K from 300 K in zero applied field by quenching the superconducting magnet in the magnetometer before cooling. After temperature stabilization at 2 K, a small magnetic field $H = 0.01$ T was applied and the time t-dependent magnetization $M(t)$ recorded. Figure 12 depicts the magnetic relaxation behavior of $Ca(Co_{1-x}Ir_x)_{2-y}As_2$ crystals with $x \geqslant 0.14$ measured with $H \parallel ab$ and $H \parallel c$, where the time dependence of the relative change $[M(t) - M(t = 0)]/M(0)$ is presented. As seen from the figure, although little relaxation is apparent for $x = 0.14$, the crystals with $x = 0.17$, 0.25, and 0.35 show strong magnetization relaxation for both ab-plane and c-axis magnetic fields. These results confirm metastable-state formation in the low-T region for $0.17 \leqslant x \leqslant 0.35$. The composition $x = 0.14$ is thus close to the boundary between the A-type AFM phase and the FM cluster-glass phase.

We note that the parent compound $CaCo_{2-y}As_2$ exhibits A-type AFM ordering with strong magnetic frustration within the J_1-J_2 Heisenberg model on a square lattice with a nearest-neighbor FM exchange interaction between the Co spins [33].

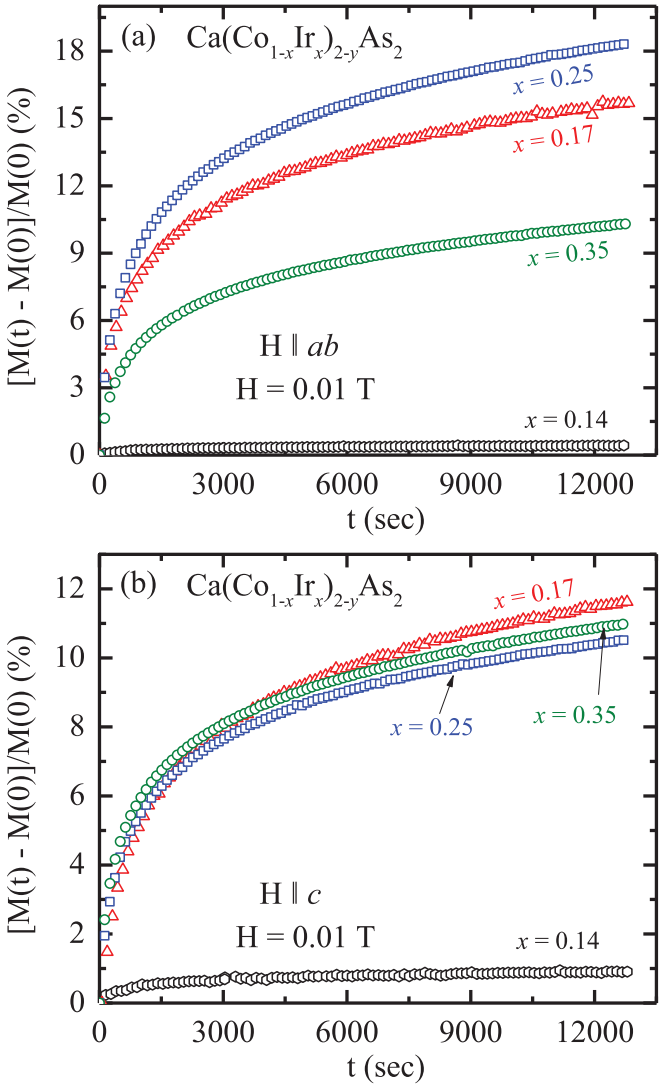

FIG. 12. Relative magnetic relaxation $[M(t) - M(0]/M(0)$ versus time t of $Ca(Co_{1-x}Ir_x)_{2-y}As_2$ crystals with $x \geqslant 0.14$ at $T = 2$ K when a small field $H = 0.01$ T is applied at $t = 0$ (a) parallel to the ab plane and (b) along the c axis.

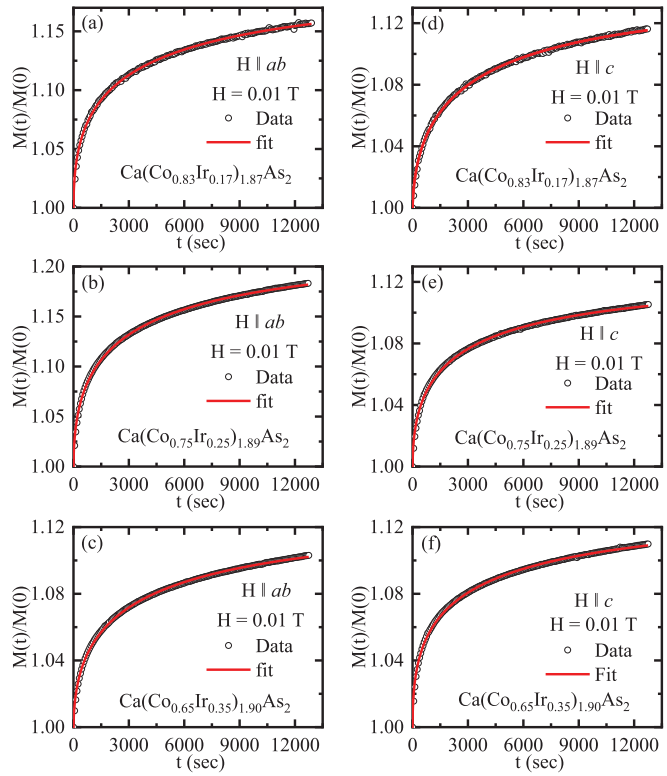

FIG. 13. (a)–(c) In-plane ($H \parallel ab$) and (d)–(f) out-of-plane ($H \parallel c$) magnetic relaxation $M(t)/M(0)$ versus time t for $x = 0.17$, 0.25, and 0.35 crystals, respectively, along with stretched exponential fits by Eq. (7).

TABLE IV. Parameters obtained from stretched exponential fits to the magnetic relaxation behavior of $Ca(Co_{1-x}Ir_x)_{2-y}As_2$ compounds with $x = 0.17$, 0.25, and 0.35.

Compound	H direction	τ (sec)	α
$Ca(Co_{0.83}Ir_{0.17})_{1.87}As_2$	$H \parallel ab$	3598(107)	0.44(1)
	$H \parallel c$	3269(108)	0.45(1)
$Ca(Co_{0.75}Ir_{0.25})_{1.89}As_2$	$H \parallel ab$	3245(87)	0.45(1)
	$H \parallel c$	2909(77)	0.45(1)
$Ca(Co_{0.65}Ir_{0.35})_{1.90}As_2$	$H \parallel ab$	3840(116)	0.46(1)
	$H \parallel c$	3189(106)	0.42(1)

Increasing the Ir concentration results in an apparent increase in the FM interaction in these systems. The Ir substitution for Co occurs randomly leading to an increase of the randomly-distributed FM exchange interactions in the crystals. Thus it is plausible that in the presence of frustration and an increase in FM correlations induced by Ir substitution, a low-T magnetically-disordered glassy state is formed for $x \geqslant 0.17$ in $Ca(Co_{1-x}Ir_x)_{2-y}As_2$. From Fig. 12, the relaxation is seen to be stronger for the magnetic field aligned in the ab plane compared to the c-axis alignment.

In glassy systems, the relaxation of the magnetization M is often described by a stretched-exponential function with the time t dependence

$$\frac{M(t)}{M(t=0)} = 1 - e^{-(t/\tau)^{\alpha}}, \tag{7}$$

where α is the stretched-exponential exponent and τ is a characteristic relaxation time [61,65]. A null value of α signifies no relaxation, whereas $\alpha = 1$ corresponds to a single magnetization relaxation time. Typically, magnetically disordered glassy systems are characterized by a distribution of energy barriers where the value of α is between 0 and 1.

The time-dependent relaxation of the magnetization of the crystals with $x = 0.17$, 0.25, and 0.35 toward saturation is indeed well described by Eq. (7), as shown in Fig. 13. The fitted parameters τ and α for each x are listed in Table IV. These results confirm the formation of a magnetically-disordered glassy state in the low-temperature region in $Ca(Co_{1-x}Ir_x)_{2-y}As_2$ crystals with $0.17 \leqslant x \leqslant 0.35$.

VI. HEAT CAPACITY

Figure 14 shows the zero-field heat capacity $C_p(T)$ of the $Ca(Co_{1-x}Ir_x)_{2-y}As_2$ crystals in the temperature range 1.8–300 K. The $C_p(T)$ data saturate with increasing T to a value at 300 K close to the classical Dulong-Petit limit $C_p = 3nR = 124.7$ J/mol K where R is the molar gas constant and here $n \approx 5$ is the number of atoms per formula unit.

The low-T $C_p(T)$ data in the temperature range 1.8 K $\leqslant T \leqslant$ 10 K for the $Ca(Co_{1-x}Ir_x)_{2-y}As_2$ crystals were analyzed using the relation

$$C_p(T) = \gamma T + \beta T^3 + \delta T^5, \tag{8}$$

where γ is the Sommerfeld coefficient associated with the itinerant electrons and the last two terms constitute the low-T lattice heat-capacity contribution. The insets in Figs. 14(a)–14(h) show $C_p(T)/T$ as a function of T^2 and the respective fits by Eq. (8). The fitted values of γ, β, and δ are listed in Table V. The γ value increases significantly from 29.6(1) to 48.3(2) mJ mol^{-1} K^{-2} with only 3.3% Ir substitution for Co in $CaCo_{1.86(2)}As_2$. This result reflects a sharp increase in the density of states at the Fermi energy $\mathcal{D}(E_F)$ with Ir substitution as determined from the relationship

$$\mathcal{D}_\gamma(E_F)\left(\frac{\text{states}}{\text{eV f.u.}}\right) = \frac{1}{2.357}\,\gamma\left(\frac{\text{mJ}}{\text{mol K}^2}\right), \tag{9}$$

where this expression for $\mathcal{D}_\gamma(E_F)$ derived from γ includes the factor of two Zeeman degeneracy of the conduction carriers. The values of $\mathcal{D}_\gamma(E_F)$ for the crystals are listed in Table V.

Low-T upturns are observed in the C_p/T versus T plots in Fig. 16 for the crystals with $x = 0.10$ and 0.14. The upturn is more pronounced for the latter composition. These upturns are not fitted well by Eq. (8) down to the lowest measured temperature and will therefore be refitted using Eq. (11) below.

TABLE V. The fitting parameters obtained from the analysis of heat-capacity data. The listed parameters are the Sommerfeld coefficient γ, the density of states at the Fermi energy $\mathcal{D}(E_F)$ derived from γ using Eq. (9), the lattice heat-capacity coefficients β and δ estimated from the low-T fit of C_p/T versus T^2 using Eq. (8), and Sommerfeld coefficient γ_D along with the Debye temperature Θ_D determined by the fit of C_p versus T data using Eqs. (10).

Compound	γ (mJ mol^{-1} K^{-2})	$\mathcal{D}(E_F)$ (states/eV f.u.)	β (mJ mol^{-1} K^{-4})	δ (μJ mol^{-1} K^{-6})	γ_D (mJ mol^{-1} K^{-2})	Θ_D (K)
$CaCo_{1.86}As_2$	29.6(1)	12.6(3)	0.391(1)	≈0	29.4(3)	357(4)
$Ca(Co_{0.967}Ir_{0.033})_{1.86}As_2$	48.3(2)	20.49(8)	0.129(8)	0.61(6)	34(2)	344(2)
$Ca(Co_{0.935}Ir_{0.065})_{1.86}As_2$	51.6(1)	21.89(4)	0.097(4)	0.80(3)	35(1)	344(2)
$Ca(Co_{0.90}Ir_{0.10})_{1.86}As_2$	62.8(1)	26.64(4)	0.025(6)	1.26(4)	36(1)	337(2)
$Ca(Co_{0.86}Ir_{0.14})_{1.87}As_2$	61.4(4)	26.1(2)	0.020(10)	1.32(7)	33(1)	331(2)
$Ca(Co_{0.83}Ir_{0.17})_{1.87}As_2$	54.4(1)	23.08(4)	0.062(4)	0.99(3)	31(1)	349(2)
$Ca(Co_{0.75}Ir_{0.25})_{1.89}As_2$	52.5(5)	22.3(2)	0.060(10)	1.11(7)	30(2)	355(2)
$Ca(Co_{0.65}Ir_{0.35})_{1.90}As_2$	47.0(1)	19.94(4)	0.066(5)	1.24(3)	27(1)	349(2)

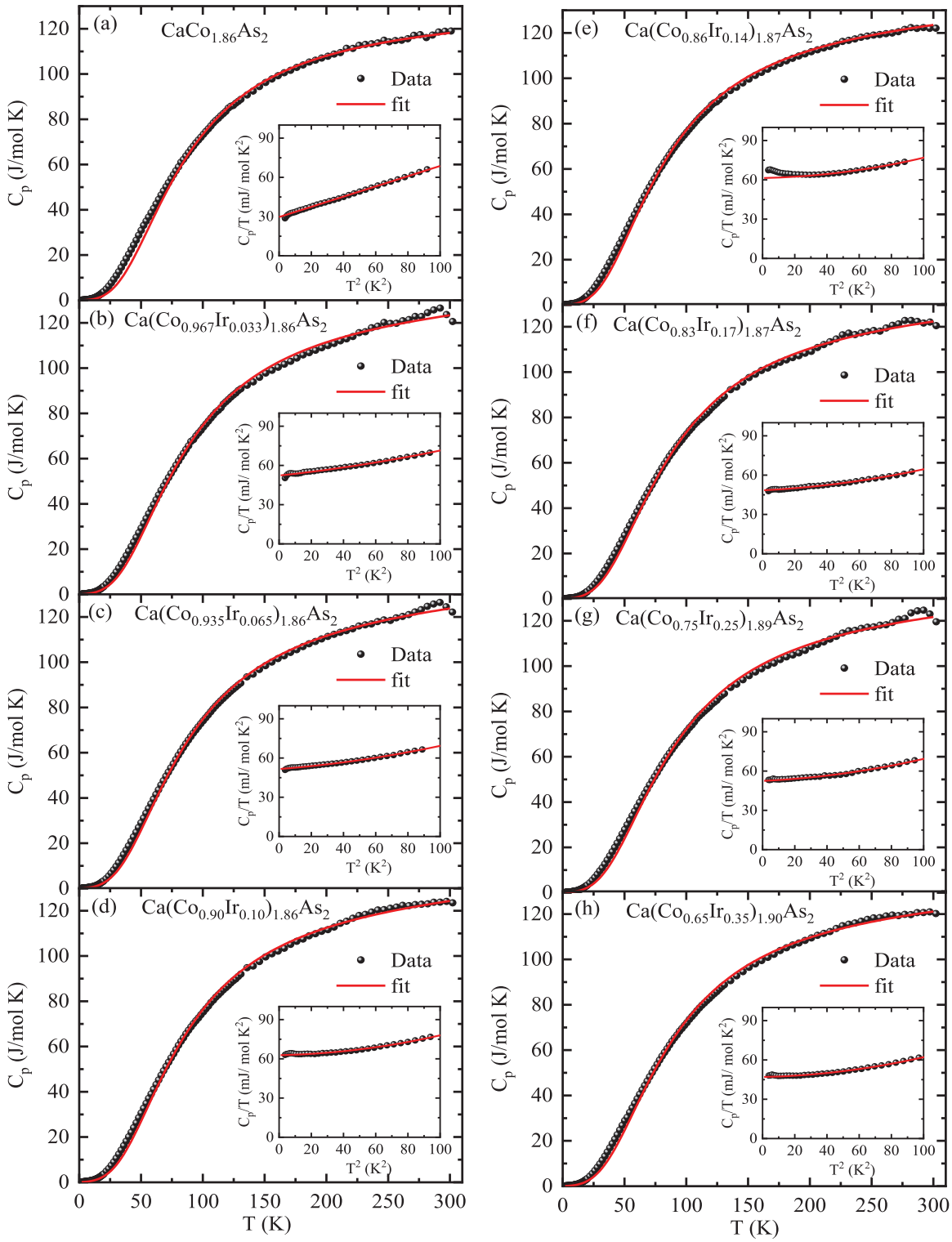

FIG. 14. Temperature T dependence of the heat-capacity C_p for $Ca(Co_{1-x}Ir_x)_{2-y}As_2$ crystals in zero field. The red solid lines are fits of the data by the Debye model using Eq. (10). Insets: C_p/T versus T^2 in the temperature range 1.8 K $\leqslant T \leqslant$ 10 K along with the fits by Eq. (8).

The $C_p(T)$ data were analyzed over the entire temperature range of the measurements using the relation

$$C_p(T) = \gamma_D T + nC_{V\,\mathrm{Debye}}(T),$$

$$C_{V\,\mathrm{Debye}}(T) = 9R\left(\frac{T}{\Theta_D}\right)^3 \int_0^{\Theta_D/T} \frac{x^4 e^x}{(e^x-1)^2} dx, \qquad (10)$$

where n is the number of atoms per formula unit, γ_D is the Sommerfeld coefficient derived from the present fit, $C_{V\,\mathrm{Debye}}$ is the Debye lattice heat capacity per mole of atoms at constant volume, and Θ_D is the Debye temperature. The fitted values of γ_D and Θ_D for all the crystals are listed in Table V. The values

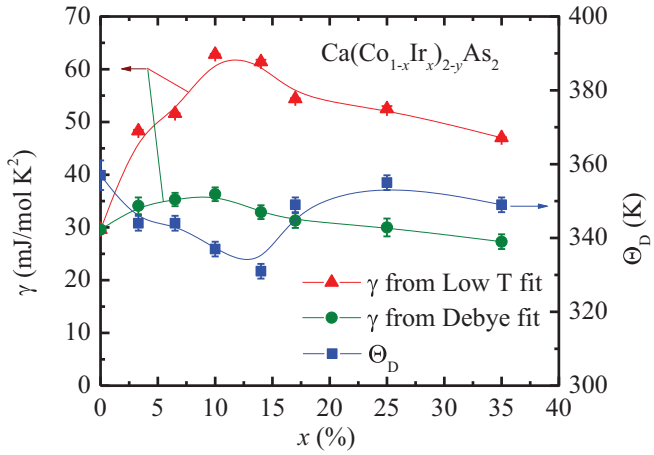

FIG. 15. Sommerfeld coefficient γ from the low-T heat-capacity fit by Eq. (8), and γ_D and Θ_D from the Debye fit in Eq. (10) for the $Ca(Co_{1-x}Ir_x)_{2-y}As_2$ crystals. The lines are guides to the eye.

of γ and γ_D are the same for the parent compound with $x = 0$ but differ significantly from each other for the Ir-substituted crystals with $x > 0$ as shown in Table V and Fig. 15, where $\gamma_D \sim \gamma/2$.

To investigate the origin of the low-T upturns in $C_p(T)/T$ versus T for the $Ca(Co_{1-x}Ir_x)_{2-y}As_2$ crystals with $x = 0.10$ and 0.14 in Fig. 16, the dependence of $C_p(T)$ on applied c-axis fields from 0 to 7 T was measured for $x = 0.10$ and 0.14 together with analogous measurements of the neighboring compositions $x = 0.065$ and 0.17. Figure 16 shows that the magnetic field strongly alters C_p/T versus T for $x = 0.14$, moderately alters those of the crystals with $x = 0.10$ and 0.17, and has almost no influence for $x = 0.065$. The low-T upturn for $x = 0.14$ is strongly suppressed by the applied field. Such types of behavior have been previously observed for different compounds with FM quantum-critical fluctuations [66,67]

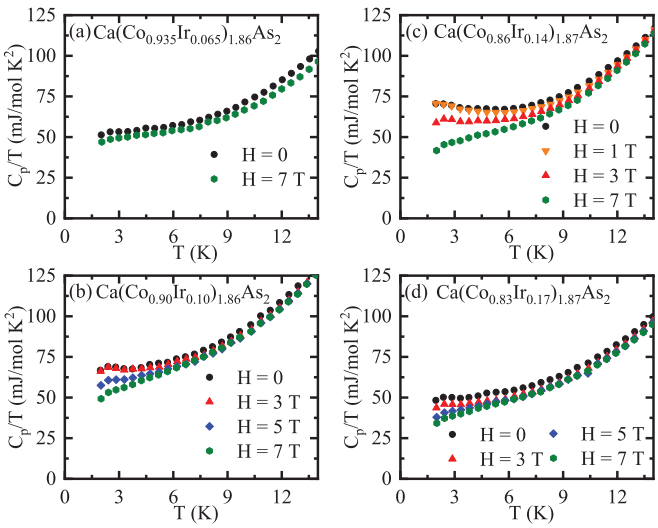

FIG. 16. C_p/T versus T behavior at different applied magnetic fields in $Ca(Co_{1-x}Ir_x)_{2-y}As_2$ crystals for (a) $x = 0.065$, (b) $x = 0.10$, (c) $x = 0.14$, and (d) $x = 0.17$.

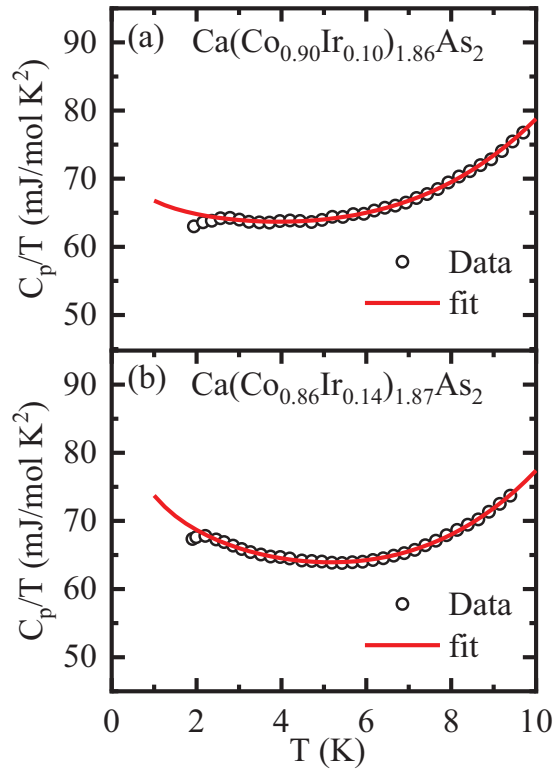

FIG. 17. Zero-field C_p/T versus T data of $Ca(Co_{1-x}Ir_x)_{2-y}As_2$ crystals with (a) $x = 0.10$ and (b) $x = 0.14$, in the temperature range 1.8 to 10 K. The solid red curves are fits by Eq. (11).

and were also recently reported to occur in isostructural $Sr(Co_{1-x}Ni_x)_2As_2$ crystals [37].

In this context, we recall that with increasing Ir substitution for Co in $CaCo_{1.86(2)}As_2$, FM interactions increase significantly and FM clustering occurs for $x \geqslant 0.17$. Furthermore, the above analyses revealed that the $x = 0.14$ composition is close to the phase boundary between the competing A-type AFM phase and magnetically-disordered FM cluster-glass phase. Thus, it seems reasonable to interpret the upturn in C_p/T versus T at low T for $x = 0.14$ as arising from FM quantum-critical fluctuations associated with a quantum-critical composition between the AFM and FM cluster-glass states.

In some systems, a $C_p/T \sim \ln T$ contribution attributed to quantum-critical fluctuations has been included to fit the low-T $C_p(T)$ data in addition to electronic and lattice heat-capacity contributions [37,68,69]. Therefore, for our crystals with $x = 0.10$ and 0.14, we analyzed the C_p/T versus T data using the relation

$$\frac{C_p(T)}{T} = \gamma_{SF} + \beta_{SF}T^2 + \delta_{SF}T^4 + \kappa \ln(T/T_{SF}), \qquad (11)$$

where γ_{SF} is the Sommerfeld coefficient determined from this fit, β_{SF} and δ_{SF} are the lattice heat-capacity coefficients from this fit, κ is the spin fluctuation coefficient, and T_{SF} is the spin fluctuation temperature. The low-T upturns seen in the data for the $x = 0.10$ and 0.14 crystals are well fitted by incorporating the latter term, as shown in Fig. 17. The fitted parameters are listed in Table. VI.

TABLE VI. Parameters obtained from fitting C_p/T versus T in the temperature range 1.8–10 K by Eq. (11) for $x = 0.10$ and 0.14.

Compound	γ_{SF} (mJ mol^{-1} K^{-2})	β_{SF} (mJ mol^{-1} K^{-4})	δ_{SF} (μJ mol^{-1} K^{-6})	κ (mJ mol^{-1} K^{-2})	T_{SF} (K)
$Ca(Co_{0.90}Ir_{0.10})_{1.86}As_2$	57.6(2)	0.06(3)	1.3(3)	−3.1(8)	18(3)
$Ca(Co_{0.86}Ir_{0.14})_{1.87}As_2$	53.2(7)	0.06(1)	1.5(1)	−7.6(4)	14(2)

An approximate phase diagram in the temperature-composition plane of the $Ca(Co_{1-x}Ir_x)_{2-y}As_2$ system is shown in Fig. 18 based on the presently-available $T_N(x)$ and $T_B(x)$ data. Also included is the concentration dependence of the spin-flop field H_{SF} which is expected to be correlated with T_N and is therefore used to help delineate the boundaries between the AFM, PM, and FMCG phases.

VII. SUMMARY

In this paper, we investigated the physical properties of Ir-substituted $Ca(Co_{1-x}Ir_x)_{2-y}As_2$ single crystals with $0 \leqslant x \leqslant 0.35$ and $0.10 \leqslant y \leqslant 0.14$ that were grown out of Co-Ir-As self flux. Room-temperature x-ray diffraction measurements showed that all the crystals form in the collapsed-tetragonal structure, as does the parent compound $CaCo_{2-y}As_2$. The SEM-EDS results showed that the vacancy concentration on the Co site is sensitive to the Ir concentration x, which changes from 7% in the parent $CaCo_{2-y}As_2$ to 5% in the 35% Ir-substituted composition. Both the tetragonal lattice parameters $a = b$ and c were found to increase nonlinearly with x, yielding a nonlinear unit cell volume versus x.

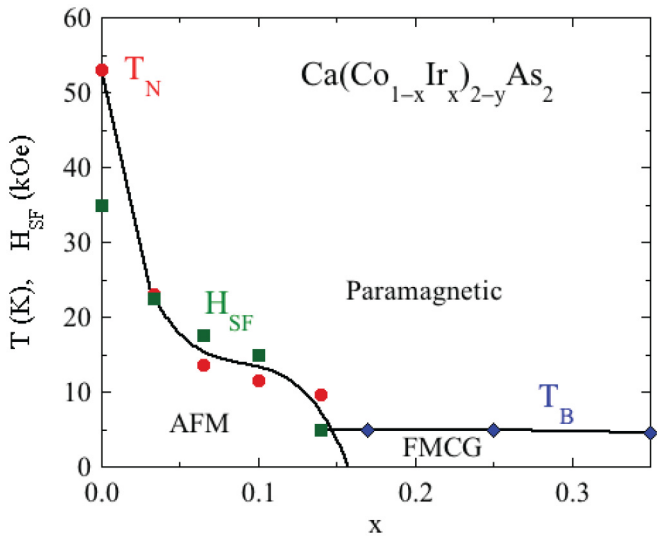

FIG. 18. Tentative phase diagram of the $Ca(Co_{1-x}Ir_x)_{2-y}As_2$ system. The Néel temperatures T_N (filled red circles), spin flop fields H_{SF} (filled green squares), and blocking temperatures T_B (filled blue diamonds) from Table II are plotted versus the Ir concentration x. The estimated phase boundaries between the A-type antiferromagntic (AFM), paramagnetic, and static ferromagnetic cluster-glass (FMCG) phases are indicated by black lines. For $x = 0.10$, static AFM and dynamic FMCG regions appear to coexist whereas, for $x = 0.14$, static AFM and both static and dynamic FMCG regions appear to coexist. For $x \geqslant 0.17$, only the static FMCG state is observed.

The temperature dependence of the static magnetic susceptibility χ shows that the A-type AFM transition temperature $T_N = 52$ K of $CaCo_{2-y}As_2$ rapidly drops to 23 K with only 3.3% Ir substitution. Increasing x dramatically enhances ferromagnetic fluctuations, both in plane and out of plane, and further decreases T_N which approaches zero for $x = 0.14$. A phase transition then occurs at $x \approx 0.16$ to a ferromagnetic cluster-glass phase for $0.17 \leqslant x \leqslant 0.35$ below a blocking temperature $T_B \lesssim 5$ K, exemplified by observations of magnetization irreversibility between zero-field-cooled and field-cooled measurements, a small spontaneous ferromagnetic component to the ordering, and spin-glass-type stretched-exponential dynamics in the time dependence of the magnetization response to a small applied field.

The zero-field heat-capacity $C_p(T)$ reveals a strong increase in the Sommerfeld heat-capacity coefficient γ with Ir substitution, signifying a corresponding increase in the electronic density of states at the Fermi energy in the Ir-substituted $Ca(Co_{1-x}Ir_x)_{2-y}As_2$ crystals. A low-temperature upturn in C_p/T versus T is observed for $x = 0.10$ and 0.14, with the strongest such contribution for $x = 0.14$, near the boundary between the A-type AFM phase and the FMCG phase. The upturn in C_p/T versus T for $x = 0.14$ is fitted well by a logarithmic temperature dependence that we associate with ferromagnetic quantum-critical spin fluctuations. The observed upturn in C_p/T versus T is strongly suppressed by an $H = 7$ T magnetic field, consistent with this interpretation.

Thus, increasing the random Ir-substitution for Co in $CaCo_{2-y}As_2$ results in a strong increase in FM interactions that in turn results in a phase transition at $x \approx 0.16$ from A-type AFM to a FMCG phase. The composition $x = 0.14$ which is close to the transition composition exhibits a signature of ferromagnetic quantum fluctuations. We infer that the FMCG phase at larger x ($x = 0.17$, 0.25, 0.35) arises from a competition between AFM and FM interactions in conjunction with crystallographic disorder accompanying Ir substitution. The properties of the Ir-substituted $Ca(Co_{1-x}Ir_x)_{2-y}As_2$ system are distinctly different from the behavior seen previously in other doped ACo_2As_2 systems. It would be interesting to study theoretically the influence of the $5d$ orbitals and spin-orbit coupling associated with the Ir atoms on the results presented in this paper.

ACKNOWLEDGMENTS

We thank B. G. Ueland for helpful comments on the manuscript. The research at Ames Laboratory was supported by the US Department of Energy, Office of Basic Energy

Sciences, Division of Materials Sciences and Engineering. Ames Laboratory is operated for the US Department of Energy by Iowa State University under Contract No. DE-AC02-07CH11358.

[1] M. Rotter, M. Tegel, and D. Johrendt, Superconductivity at 38 K in the Iron Arsenide $(Ba_{1-x}K_x)Fe_2As_2$, Phys. Rev. Lett. **101**, 107006 (2008).

[2] D. C. Johnston, The puzzle of high temperature superconductivity in layered iron pnictides and chalcogenides, Adv. Phys. **59**, 803 (2010).

[3] P. C. Canfield and S. L. Bud'ko, FeAs-Based Superconductivity: A Case Study of the Effects of Transition Metal Doping on $BaFe_2As_2$, Annu. Rev. Condens. Matter Phys. **1**, 27 (2010).

[4] J. Paglione and R. L. Greene, High-temperature superconductivity in iron-based materials, Nat. Phys. **6**, 645 (2010).

[5] R. M. Fernandes, D. K. Pratt, W. Tian, J. Zarestky, A. Kreyssig, S. Nandi, M. G. Kim, A. Thaler, N. Ni, P. C. Canfield, R. J. McQueeney, J. Schmalian, and A. I. Goldman, Unconventional pairing in the iron arsenide superconductors, Phys. Rev. B **81**, 140501(R) (2010).

[6] G. R. Stewart, Superconductivity in iron compounds, Rev. Mod. Phys. **83**, 1589 (2011).

[7] D. J. Scalapino, A common thread: The pairing interaction for unconventional superconductors, Rev. Mod. Phys. **84**, 1383 (2012).

[8] P. Dai, J. Hu, and E. Dagotto, Magnetism and its microscopic origin in iron-based high-temperature superconductors, Nat. Phys. **8**, 709 (2012).

[9] E. Dagotto, The unexpected properties of alkali metal iron selenide superconductors, Rev. Mod. Phys. **85**, 849 (2013).

[10] P. Dai, Antiferromagnetic order and spin dynamics in iron-based superconductors, Rev. Mod. Phys. **87**, 855 (2015).

[11] A. Kreyssig, M. A. Green, Y. Lee, G. D. Samolyuk, P. Zajdel, J. W. Lynn, S. L. Bud'ko, M. S. Torikachvili, N. Ni, S. Nandi, J. B. Leão, S. J. Poulton, D. N. Argyriou, B. N. Harmon, R. J. McQueeney, P. C. Canfield, and A. I. Goldman, Pressure-induced volume-collapsed tetragonal phase of $CaFe_2As_2$ as seen via neutron scattering, Phys. Rev. B **78**, 184517 (2008).

[12] A. I. Goldman, A. Kreyssig, K. Prokeš, D. K. Pratt, D. N. Argyriou, J. W. Lynn, S. Nandi, S. A. J. Kimber, Y. Chen, Y. B. Lee, G. Samolyuk, J. B. Leão, S. J. Poulton, S. L. Bud'ko, N. Ni, P. C. Canfield, B. N. Harmon, and R. J. McQueeney, Lattice collapse and quenching of magnetism in $CaFe_2As_2$ under pressure: A single-crystal neutron and x-ray diffraction investigation, Phys. Rev. B **79**, 024513 (2009).

[13] S. Kawasaki, T. Tabuchi, X. F. Wang, X. H. Chen, and G.-q. Zheng, Pressure-induced unconventional superconductivity near a quantum critical point in $CaFe_2As_2$, Supercond. Sci. Technol. **23**, 054004 (2010).

[14] For a review of collapsed- and uncollapsed-tetragonal materials, see Sec. VIII of V. K. Anand, P. K. Perera, A. Pandey, R. J. Goetsch, A. Kreyssig, and D. C. Johnston, Crystal growth and physical properties of $SrCu_2As_2$, $SrCu_2Sb_2$ and $BaCu_2Sb_2$, Phys. Rev. B **85**, 214523 (2012).

[15] K. Sasmal, B. Lv, B. Lorenz, A. M. Guloy, F. Chen, Y.-Y. Xue, and C.-W. Chu, Superconducting Fe-based Compounds $(A_{1-x}Sr_x)Fe_2As_2$ with $A =$ K and Cs with Transition Temperatures up to 37 K, Phys. Rev. Lett. **101**, 107007 (2008).

[16] A. Leithe-Jasper, W. Schnelle, C. Geibel, and H. Rosner, Superconducting State in $SrFe_{2-x}Co_xAs_2$ by Internal Doping of the Iron Arsenide Layers, Phys. Rev. Lett. **101**, 207004 (2008).

[17] N. Kumar, S. Chi, Y. Chen, K. G. Rana, A. K. Nigam, A. Thamizhavel, W. Ratcliff, II, S. K. Dhar, and J. W. Lynn, Evolution of the bulk properties, structure, magnetic order, and superconductivity with Ni doping in $CaFe_{2-x}Ni_xAs_2$, Phys. Rev. B **80**, 144524 (2009).

[18] Z. Ren, Q. Tao, S. Jiang, C. Feng, C. Wang, J. Dai, G. Cao, and Z. Xu, Superconductivity Induced by Phosphorus Doping and Its Coexistence with Ferromagnetism in $EuFe_2(As_{0.7}P_{0.3})_2$, Phys. Rev. Lett. **102**, 137002 (2009).

[19] M. Rotter, M. Pangerl, M. Tegel, and D. Johrendt, Superconductivity and crystal structures of $(Ba_{1-x}K_x)Fe_2As_2$ $(x = 0 - 1)$, Angew. Chem., Int. Ed. **47**, 7949 (2008).

[20] Z. Bukowski, S. Weyeneth, R. Puzniak, J. Karpinski, and B. Batlogg, Bulk superconductivity at 2.6 K in undoped $RbFe_2As_2$, Physica C **470**, S328 (2010).

[21] A. S. Sefat, D. J. Singh, R. Jin, M. A. McGuire, B. C. Sales, and D. Mandrus, Renormalized behavior and proximity of $BaCo_2As_2$ to a magnetic quantum critical point, Phys. Rev. B **79**, 024512 (2009).

[22] V. K. Anand, D. G. Quirinale, Y. Lee, B. N. Harmon, Y. Furukawa, V. V. Ogloblichev, A. Huq, D. L. Abernathy, P. W. Stephens, R. J. McQueeney, A. Kreyssig, A. I. Goldman, and D. C. Johnston, Crystallography and physical properties of $BaCo_2As_2$, $Ba_{0.94}K_{0.06}Co_2As_2$, and $Ba_{0.78}K_{0.22}Co_2As_2$, Phys. Rev. B **90**, 064517 (2014).

[23] A. Pandey, D. G. Quirinale, W. Jayasekara, A. Sapkota, M. G. Kim, R. S. Dhaka, Y. Lee, T. W. Heitmann, P. W. Stephens, V. Ogloblichev, A. Kreyssig, R. J. McQueeney, A. I. Goldman, A. Kaminski, B. N. Harmon, Y. Furukawa, and D. C. Johnston, Crystallographic, electronic, thermal, and magnetic properties of single-crystal $SrCo_2As_2$, Phys. Rev. B **88**, 014526 (2013).

[24] D. G. Quirinale, V. K. Anand, M. G. Kim, A. Pandey, A. Huq, P. W. Stephens, T. W. Heitmann, A. Kreyssig, R. J. McQueeney, D. C. Johnston, and A. I. Goldman, Crystal and magnetic structure of $CaCo_{1.86}As_2$ studied by x-ray and neutron diffraction, Phys. Rev. B **88**, 174420 (2013).

[25] V. K. Anand, R. S. Dhaka, Y. Lee, B. N. Harmon, A. Kaminski, and D. C. Johnston, Physical properties of metallic antiferromagnetic $CaCo_{1.86}As_2$ single crystals, Phys. Rev. B **89**, 214409 (2014).

[26] B. Li, B. G. Ueland, W. T. Jayasekara, D. L. Abernathy, N. S. Sangeetha, D. C. Johnston, Q.-P. Ding, Y. Furukawa, P. P. Orth, A. Kreyssig, A. I. Goldman, and R. J. McQueeney, Competing magnetic phases and itinerant magnetic frustration in $SrCo_2As_2$, Phys. Rev. B **100**, 054411 (2019).

[27] W. Jayasekara, Y. Lee, A. Pandey, G. S. Tucker, A. Sapkota, J. Lamsal, S. Calder, D. L. Abernathy, J. L. Niedziela, B. N. Harmon, A. Kreyssig, D. Vaknin, D. C. Johnston, A. I. Goldman, and R. J. McQueeney, Stripe Antiferromagnetic Spin Fluctuations in $SrCo_2As_2$, Phys. Rev. Lett. **111**, 157001 (2013).

[28] P. Wiecki, V. Ogloblichev, A. Pandey, D. C. Johnston, and Y. Furukawa, Coexistence of antiferromagnetic and ferromagnetic spin correlations in $SrCo_2As_2$ revealed by ^{59}Co and ^{75}As NMR, Phys. Rev. B **91**, 220406(R) (2015).

[29] Y. Li, Z. Yin, Z. Liu, W. Wang, Z. Xu, Y. Song, L. Tian, Y. Huang, D. Shen, D. L. Abernathy, J. L. Niedziela, R. A. Ewings, T. G. Perring, D. M. Pajerowski, M. Matsuda, P. Bourges, E. Mechthild, Y. Su, and P. Dai, Coexistence of Ferromagnetic and Stripe Antiferromagnetic Spin Fluctuations in $SrCo_2As_2$, Phys. Rev. Lett. **122**, 117204 (2019).

[30] P. Wiecki, B. Roy, D. C. Johnston, S. L. Bud'ko, P. C. Canfield, and Y. Furukawa, Competing Magnetic Fluctuations in Iron Pnictide Superconductors: Role of Ferromagnetic Spin Correlations Revealed by NMR, Phys. Rev. Lett **115**, 137001 (2015).

[31] B. Cheng, B. F. Hu, R. H. Yuan, T. Dong, A. F. Fang, Z. G. Chen, G. Xu, Y. G. Shi, P. Zheng, J. L. Luo, and N. L. Wang, Field induced spin flop transitions in single-crystalline $CaCo_{2-y}As_2$, Phys. Rev. B **85**, 144426 (2012).

[32] J. J. Ying, Y. J. Yan, A. F. Wang, Z. J. Xiang, P. Cheng, G. J. Ye, and X. H. Chen, Metamagnetic transition in $Ca_{1-x}Sr_xCo_2As_2$ ($x = 0$ and 0.1) single crystals, Phys. Rev. B **85**, 214414 (2012).

[33] A. Sapkota, B. G. Ueland, V. K. Anand, N. S. Sangeetha, D. L. Abernathy, M. B. Stone, J. L. Niedziela, D. C. Johnston, A. Kreyssig, A. I. Goldman, and R. J. McQueeney, Effective One-Dimensional Coupling in the Highly Frustrated Square-Lattice Itinerant Magnet $CaCo_{2-y}As_2$, Phys. Rev. Lett. **119**, 147201 (2017).

[34] J. J. Ying, J. C. Liang, X. G. Luo, Y. J. Yan, A. F. Wang, P. Cheng, G. J. Ye, J. Q. Ma, and X. H. Chen, The magnetic phase diagram of $Ca_{1-x}Sr_xCo_{2-y}As_2$ single crystals, Europhys. Lett. **104**, 67005 (2013).

[35] N. S. Sangeetha, V. Smetana, A.-V. Mudring, and D. C. Johnston, Anomalous Composition-Induced Crossover in the Magnetic Properties of the Itinerant-Electron Antiferromagnet $Ca_{1-x}Sr_xCo_{2-y}As_2$, Phys. Rev. Lett. **119**, 257203 (2017).

[36] B. Li, Y. Sizyuk, N. S. Sangeetha, J. M. Wilde, P. Das, W. Tian, D. C. Johnston, A. I. Goldman, A. Kreyssig, P. P. Orth, R. J. McQueeney, and B. G. Ueland, Antiferromagnetic stacking of ferromagnetic layers and doping-controlled phase competition in $Ca_{1-x}Sr_xCo_{2-y}As_2$, Phys. Rev. B **100**, 024415 (2019).

[37] N. S. Sangeetha, L.-L. Wang, A. V. Smirnov, V. Smetana, A.-V. Mudring, D. D. Johnson, M. A. Tanatar, R. Prozorov, and D. C. Johnston, Non-Fermi-liquid types of behavior associated with a magnetic quantum critical point in $Sr(Co_{1-x}Ni_x)_2As_2$ single crystals, Phys. Rev. B **100**, 094447 (2019).

[38] Y. Li, Z. Liu, Z. Xu, Y. Song, Y. Huang, D. Shen, N. Ma, A. Li, S. Chi, M. Frontzek, H. Cao, Q. Huang, W. Wang, Y. Xie, R. Zhang, Y. Rong, W. A. Shelton, D. P. Young, J. F. DiTusa, and P. Dai, Flat-band magnetism and helical magnetic order in Ni-doped $SrCo_2As_2$, Phys. Rev. B **100**, 094446 (2019).

[39] J. M. Wilde, A. Kreyssig, D. Vaknin, N. S. Sangeetha, B. Li, W. Tian, P. P. Orth, D. C. Johnston, B. G. Ueland, and R. J. McQueeney, Helical magnetic ordering in $Sr(Co_{1-x}Ni_x)_2As_2$, Phys. Rev. B **100**, 161113(R) (2019).

[40] S. Shen, S. Feng, Z. Lin, Z. Wang, and W. Zhong, Ferromagnetic behavior induced by La-doping in $SrCo_2As_2$, J. Mater. Chem. C **6**, 8076 (2018).

[41] S. Shen, W. Zhong, D. Li, Z. Lin, Z. Wang, X. Gu, and S. Feng, Itinerant ferromagnetism induced by electron doping in $SrCo_2As_2$, Inorg. Chem. Commun. **103**, 25 (2019).

[42] W. T. Jayasekara, A. Pandey, A. Kreyssig, N. S. Sangeetha, A. Sapkota, K. Kothapalli, V. K. Anand, W. Tian, D. Vaknin, D. C. Johnston, R. J. McQueeney, A. I. Goldman, and B. G. Ueland, Suppression of magnetic order in $CaCo_{1.86}As_2$ with Fe substitution: Magnetization, neutron diffraction, and x-ray diffraction studies of $Ca(Co_{1-x}Fe_x)_yAs_2$, Phys. Rev. B **95**, 064425 (2017).

[43] M. Smidman, M. B. Salamon, H. Q. Yuan, and D. F. Agterberg, Superconductivity and spin-orbit coupling in non-centrosymmetric materials: a review, Rep. Prog. Phys. **80**, 036501 (2017).

[44] M. A. Laguna-Marco, D. Haskel, N. Souza-Neto, J. C. Lang, V. V. Krishnamurthy, S. Chikara, G. Cao, and M. van Veenendaal, Orbital Magnetism and Spin-Orbit Effects in the Electronic Structure of $BaIrO_3$, Phys. Rev. Lett. **105**, 216407 (2010).

[45] K. K. Ng and M. Sigrist, The role of spin-orbit coupling for the superconducting state in Sr_2RuO_4, Europhys. Lett. **49**, 473 (2000).

[46] D. Rhodes, S. Das, Q. R. Zhang, B. Zeng, N. R. Pradhan, N. Kikugawa, E. Manousakis, and L. Balicas, Role of spin-orbit coupling and evolution of the electronic structure of WTe_2 under an external magnetic field, Phys. Rev. B **92**, 125152 (2015).

[47] K. W. Plumb, J. P. Clancy, L. J. Sandilands, V. V. Shankar, Y. F. Hu, K. S. Burch, H.-Y. Kee, and Y.-J. Kim, α-$RuCl_3$: A spin-orbit assisted Mott insulator on a honeycomb lattice, Phys. Rev. B **90**, 041112(R) (2014).

[48] M. Ma, P. Bourges, Y. Sidis, Y. Xu, S. Li, B. Hu, J. Li, F. Wang, and Y. Li, Prominent Role of Spin-Orbit Coupling in FeSe Revealed by Inelastic Neutron Scattering, Phys. Rev. X **7**, 021025 (2017).

[49] APEX3, Bruker AXS Inc., Madison, Wisconsin, USA, 2015.

[50] SAINT, Bruker AXS Inc., Madison, Wisconsin, USA, 2015.

[51] L. Krause, R. Herbst-Irmer, G. M. Sheldrick, and D. J. Stalke, J. Appl. Crystallogr. **48**, 3 (2015).

[52] G. M. Sheldrick, SHELTX – Integrated space-group and crystal-structure determination, Acta Crystallogr. A **71**, 3 (2015).

[53] G. M. Sheldrick, Crystal structure refinement with SHELXL, Acta Crystallogr. Sect. C: Struct. Chem. **C71**, 3 (2015).

[54] K. Momma and F. Izumi, *VESTA 3* for three-dimensional visualization of crystal, volumetric and morphology data, J. Appl. Cryst. **44**, 1272 (2011).

[55] M. E. Fisher, Relation between the specific heat and susceptibility of an antiferromagnet, Philos. Mag. **7**, 1731 (1962).

[56] S. Pakhira, C. Mazumdar, R. Ranganathan, and S. Giri, Magnetic phase inhomogeneity in frustrated intermetallic compound $Sm_2Ni_{0.87}Si_{2.87}$, J. Alloys Compd. **742**, 391 (2018).

[57] D. X. Li, S. Nimori, Y. Shiokawa, Y. Haga, E. Yamamoto, and Y. Onuki, Ferromagnetic cluster glass behavior in U_2IrSi_3, Phys. Rev. B **68**, 172405 (2003).

[58] R. S. Freitas, L. Ghivelder, F. Damay, F. Dias, and L. F. Cohen, Magnetic relaxation phenomena and cluster glass properties

of $La_{0.7-x}Y_xCa_{0.3}MnO_3$ manganites, Phys. Rev. B **64**, 144404 (2001).

[59] D. N. H. Nam, K. Jonason, P. Nordblad, N. V. Khiem, and N. X. Phuc, Coexistence of ferromagnetic and glassy behavior in the $La_{0.5}Sr_{0.5}CoO_3$ perovskite compound, Phys. Rev. B **59**, 4189 (1999).

[60] V. K. Anand, D. T. Adroja, and A. D. Hillier, Ferromagnetic cluster spin-glass behavior in $PrRhSn_3$, Phys. Rev. B **85**, 014418 (2012).

[61] J. A. Mydosh, *Spin Glasses: An Experimental Introduction* (Taylor & Francis, London, 1993).

[62] K. Binder and A. P. Young, Spin glasses: Experimental facts, theoretical concepts, and open questions, Rev. Mod. Phys. **58**, 801 (1986).

[63] P. Nordblad, P. Svedlindh, L. Lundgren, and L. Sandlund, Time decay of the remanent magnetization in a Cu*Mn* spin glass, Phys. Rev. B **33**, 645(R) (1986).

[64] D. Chu, G. G. Kenning, and R. Orbach, Dynamic Measurements in a Heisenberg Spin Glass: CuMn, Phys. Rev. Lett. **72**, 3270 (1994).

[65] D. C. Johnston, Stretched exponential relaxation arising from a continuous sum of exponential decays, Phys. Rev. B **74**, 184430 (2006).

[66] L. S. Wu, M. S. Kim, K. Park, A. M. Tsvelik, and M. C. Aronson, Quantum critical fluctuations in layered YFe_2Al_{10}, Proc. Natl. Acad. Sci. USA **111**, 14088 (2014).

[67] M. Nicklas, M. Brando, G. Knebel, F. Mayr, W. Trinkl, and A. Loidl, Non-Fermi-Liquid Behavior at a Ferromagnetic Quantum Critical Point in Ni_xPd_{1-x}, Phys. Rev. Lett. **82**, 4268 (1999).

[68] P. Fulde and A. Luther, Effects of impurities on spin fluctuations in almost ferromagnetic metals, Phys. Rev. **170**, 570 (1968).

[69] A. J. Millis, Effect of a nonzero temperature on quantum critical points in itinerant fermion systems, Phys. Rev. B **48**, 7183 (1993).